Als Prüfungsexemplar genehmigt

Bollen

Karlsruhe Institute of Technology

Analysis and inversion of SV-wave anisotropy in a crosswell setting

Analyse und Inversion von SV-Wellen Anisotropie in einer Transmissionsgeometrie

Master's Thesis of
Sarah Beraus

Department of Physics
Geophysical Institute
Karlsruhe Institute for Technology

Reviewer: Prof. Dr. Thomas Bohlen
Second reviewer: apl. Prof. Dr. Joachim Ritter

November 1, 2021

Erklärung zur Selbstständigkeit

Ich versichere wahrheitsgemäß, die Arbeit selbstständig verfasst, alle benutzten Hilfsmittel vollständig und genau angegeben und alles kenntlich gemacht zu haben, was aus Arbeiten anderer unverändert oder mit Abänderungen entnommen wurde sowie die Satzung des KIT zur Sicherung guter wissenschaftlicher Praxis in der jeweils gültigen Fassung beachtet zu haben.

Ort, Datum: _____ Unterschrift: _____

Abstract

Crosswell seismic experiments provide an outstanding opportunity to obtain detailed information about the subsurface and to study anisotropy due to high source frequencies and the transmission geometry. A common form of anisotropy is given by a vertically transverse isotropic (VTI) medium which consists of fine horizontal layers. In order to study the effects of such a medium and attenuation on the SV-waves, I forward simulate the respective wavefields based on realistic wave velocities which were obtained though a traveltime tomography by von Ketelhodt et al. (2019). Their study discovered significant S-wave anisotropy and the lack thereof in case of the P-wave. This allows to perform reconstruction tests of a low-velocity anomaly where I invert for the isotropic or anisotropic S-wave velocities only while keeping the P-wave velocities and density constant. With a gradient parameterization in terms of the velocities v_{P}, $v_{\mathrm{P,hor}}$, v_{SV}, $v_{\mathrm{SV}}(45°)$ and the density ρ, both the vertical and horizontal resolution of the isotropic inversions prove to be superior compared to the VTI case. However, it is also shown that an unfitting assumption about the subsurface properties of anisotropy and viscoelasticity might yield cycle skipping and will, thus, prohibit the inversion to converge to the global minimum of the misfit function. Possible crosstalk between the SV-wave velocity parameters seems to be, if existent at all, in the order of the inversion artifacts' magnitude. Future studies should investigate how the VTI P/SV-case FWI can be improved regarding the resolution and applied to field data.

Zusammenfassung

Seismische Bohrloch-Experimente bieten aufgrund der hohen Quellfrequenzen und der Transmissionsgeometrie eine außergewöhnliche Gelegenheit detaillierte Informationen über den Untergrund zu erhalten und Anisotropie zu studieren. Eine häufig vorkommende Form der Anisotropie ist die des vertikal transversen (VTI) Mediums, welches aus feinen horizontalen Schichten besteht. Um die Effekte eines solchen Mediums und von Dämpfung auf die SV-Wellen zu untersuchen, modelliere ich die entsprechenden Wellenfelder basierend auf realistischen Wellengeschwindigkeiten, die in einer Laufzeitentomographie von von Ketelhodt et al. (2019) bestimmt wurden. Deren Studie entdeckte signifikante S-Welle Anisotropie und deren Fehlen im Falle der P-Welle. Das erlaubt Rekonstruktionstests einer Niedergeschwindigkeitsanomalie, in denen ich lediglich für die isotrope und anisotropen S-Wellen Geschwindigkeiten invertiere. Bei einer Parameterisierung des Gradient hinsichtlich der Geschwindigkeiten v_{P}, $v_{\mathrm{P,hor}}$, v_{SV}, $v_{\mathrm{SV}}(45°)$ und der Dichte ρ, erweisen sich sowohl die vertikale als auch die horizontale Auflösung der isotropen Inversion derer des VTI Falls überlegen. Jedoch wird auch gezeigt, dass eine unpassende Annahme über die Eigenschaften des Untergrunds bezüglich Anisotropie und Viskoelastizität zu *cycle skipping* führen kann und somit die Konvergenz der Inversion hin zum globalen Minimum der *misfit* Funktion verhindert. Möglicher *crosstalk* zwischen den SV-Wellen Geschwindigkeitsparametern scheint, falls überhaupt existent, in der Größenordnung der Inversinsartefakte zu sein. Künftige Studien sollten untersuchen, wie das Auflösungsvermögen der VTI Wellenforminversion im P/SV-Fall verbessert werden und auf Felddaten angewendet werden kann.

Danksagung

Zunächst möchte ich mich bei Professor Thomas Bohlen für die Betreuung dieser Masterarbeit und dabei vor allem für die Diskussion möglicher Lösungsansätze bedanken. Weiter gilt mein Dank Professor Joachim Ritter als Koreferent.

Außerdem möchte ich der gesamten Arbeitsgruppe für die wöchentlichen Diskussionen der Masterarbeitsthemen danken. Die dabei gesammelten Ideen und erhaltenen Hinweise waren sehr hilfreich. Besonderer Dank geht hierbei an Thomas Hertweck und Lars Houpt, die die Diskussionrunden moderierten und somit eine Plattform dafür boten, das Pandemie bedingt fehlende Arbeitsgruppenleben zu kompensieren.

Weiterer Dank gebührt Thomas Hertweck, Lars Houpt und Yudi Pan für das Korrekturlesen meiner Thesis. Die Hinweise zur besseren Verständlichkeit und die sprachlichen Verbesserungsvorschläge waren äußerst wertvoll.

Ein großer Dank geht an meine Kommilitoninnen und Kommilitonen. Die gemeinsamen virtuellen Kaffeepausen und der dabei stattfindende Austausch über die jeweiligen Fortschritte diverser Projekte war stets eine willkommene Abwechslung. Im Besonderen möchte ich hierbei Benedikt Braszus, Amelie Nüsse, María Urquizar Carmona, Vincent van der Heiden und Konstantin Drach danken, die immer ein offenes Ohr für mich hatten.

Zu guter Letzt möchte ich mich bei meiner Familie bedanken, die mich stets auf meinem Weg unterstützt hat.

Contents

List of Figures

List of Tables

1. Introduction

A crosswell setting provides an outstanding possibility to obtain fine-scale information about the subsurface between two or more boreholes. Moreover, it allows to determine wave velocities at different angles and hence is ideal to study anisotropy. Past studies of traveltime tomography exploit the transmission geometry with its dense ray coverage and high source frequencies to obtain a detailed image of the subsurface and to investigate it in the context of site characterization regarding, for instance, aquifers (von Ketelhodt et al., 2018), geothermal sites (Gaucher et al., 2020) as well as oil and gas reservoirs (Bauer et al., 2003, Zhang et al., 2012).

Methodological assessments of crosshole settings were done in the framework of traveltime tomography by McMechan (1983) who investigated the convergence and resolution of the inversion of synthetic data. Rao and Wang (2005) developed ideas on how to handle issues like properly setting geological constraints. Von Ketelhodt et al. (2018) applied cross-gradient constraints to ensure structural similarity between the final models that will serve as the basis for investigations regarding anisotropic FWI of crosswell seismic data in this work.

Compared to traveltime tomography, full-waveform inversion (FWI) provides a better resolution of about half a wavelength, because it considers the entire information contained in the waveforms and not only the onset times of certain phases. The method was first introduced by Tarantola (1984) and has since been applied to problems on a wide range of scales, for instance, in medical imaging (Kühn, 2018), near-surface seismics (Krampe, 2018), reflection seismics (Virieux and Operto, 2009, Warner et al., 2013) and in seismology (Tromp, 2020). This is made possible by modern high performance computers as well as efficient forward solvers and local optimization algorithms that mitigate the issue of higher computational costs compared to traveltime tomography.

Crosshole studies using FWI are usually accompanied by the application of anisotropic wave theory as the boreholes themselves pose a source of anisotropy. In most cases transverse isotropic (TI) media form the theoretical setting. Pratt et al. (2005) show in an acoustic frequency domain approach that an isotropic and an anisotropic FWI match the data equally well, though the anisotropic model is significantly smoother than expected, i.e., velocity contrasts are less strong than in the isotropic inversion. A later frequency domain study by Hadden and Pratt (2017) uses synthetic crosshole data and assumes a tilted transverse isotropic (TTI) medium to demonstrate that the effect of parameter crosstalk can be mitigated by applying a Gaussian smoothing filter before FWI in case of a monoparameter inversion. The idea to invert for one parameter only in the anisotropic case is also suggested through studies by Gholami et al. (2013).

Barnes et al. (2008) assess the feasibility of an anisotropic FWI in a crosswell setting in the time domain. For a vertically transverse isotropic (VTI) medium, they use a synthetic dataset in a cylindrical coordinate system with a radial and vertical component

and added Gaussian noise. It is shown that a parameterization with vertical velocities of the P- and S-wave, density and the Thomsen parameters ε and δ yields robust results. Kamath and Tsvankin (2014) developed an elastic time-domain FWI approach for 2D VTI media in a crosswell setting. They discuss the gradient computation, apply a parameterization in terms of velocities, i.e., vertical, horizontal and NMO velocities, and perform a sensitivity analysis. According to the study, the acquisition geometry and aperture highly influence the inversion result. Another study applying an elastic FWI to crosshole data from a VTI medium was done by Singh et al. (2020), which yields high-resolution models. They constrain the inversion based on rock-physics relationships in form of a regularization term. Further, the multi-scale approach and an image-guided smoothing algorithm is applied. The latter allows to handle the lateral heterogeneity proposed by the boreholes.

At the high frequencies that are used in crosshole experiments, attenuation should not be neglected. Charara and Barnes (2016), therefore, test an isotropic, viscoelastic FWI. It is shown that the viscoelastic parameters, i.e., the quality factor Q for both the P- and the S-wave, cannot be well recovered, but have a big influence on the determination of the elastic parameters.

In this work the effects of anisotropy and viscoelasticity on the SV-waves is investigated in a crosswell setting. The goal is to develop a suitable VTI gradient formulation for the P/SV-case and test its performance in an simple and a realistic setting. Firstly, I introduce the theoretical foundation of anisotropic wave propagation, more precisely, in vertically transverse isotropic (VTI) media. This also includes aspects of the numerical implementation and the gradient calculation and parameterization in the inversion. Secondly, I present the field data and traveltime tomographies that were conducted by von Ketelhodt et al. (2018, 2019) and that serve as a starting point for my investigations. Thirdly, the effects of anisotropy and viscoelasticity on the forward modeled wavefield are studied based on the tomography models. Eventually, synthetic inversion tests, that encompass reconstruction and crosstalk tests, reveal the limits of the elastic, anisotropic inversion method regarding the SV-waves with the chosen parameterization.

2. Theoretical background

2.1 Seismic wave propagation in anisotropic media

Wave propagation is partly expressed by the equation of conservation of momentum, which in the context of linear elasticity theory is often given in the so-called stress-velocity formulation. It can be derived from Newton's law of motion in its strong formulation

$$\rho\,\dot{\vec{v}} = \bigtriangledown \cdot \sigma + \vec{f} \Leftrightarrow \rho\,\dot{v}_i = \frac{\partial \sigma_{ij}}{\partial x_j} + f_i \tag{2.1}$$

with ρ being the density, $\vec{v}$ the particle velocity, σ the stress and $\vec{f}$ a force density, together with the stress-strain relation for elastic media (see Equation 2.2).
In the following, seismic anisotropy is introduced and characterized both by its observable effects and mathematical description. Then the necessary constitutive equations to describe wave propagation are derived for the anisotropic elastic and viscoelastic case.

2.1.1 Stress-strain relation and stiffness tensor

In linear elasticity theory, the stress-strain relation for elastic media is given by

$$\sigma_{ij} = C_{ijkl}\,\epsilon_{kl} \qquad (i,j,k,l = 1,2,3) \tag{2.2}$$

using Einstein summation convention, where σ_{ij} are the stress tensor components, C_{ijkl} are the stiffness tensor components, i.e., the elastic constants, and ϵ_{kl} are the components of the deformation tensor. The latter is usually expressed by

$$\epsilon_{kl} = \frac{1}{2}\left(\frac{\partial\, u_k}{\partial\, x_l} + \frac{\partial\, u_l}{\partial\, x_k}\right) \qquad (k,l = 1,2,3) \tag{2.3}$$

with the partial derivatives of the displacement components u_i with respect to space being in the order of 10^{-6}, i.e., small deformation is assumed.

The stiffness tensor C_{ijkl} is a tensor of fourth order with 81 components. However, in the most general anisotropic case the number of components decreases to only 21 independent components if the symmetry of the stress ($\sigma_{ij} = \sigma_{ji}$) and the deformation tensor ($\epsilon_{kl} = \epsilon_{lk}$) as well as the tensors' invariants and quantities of conservation are taken into account. This allows to write the stiffness tensor as a 6×6 matrix using Voigt's notation (Voigt, 1910) by which the number of indices is reduced. This is achieved by renaming them according to $11 \rightarrow 1, 22 \rightarrow 2, 33 \rightarrow 3, 23 \rightarrow 4, 13 \rightarrow 5, 12 \rightarrow 6$, such that the stress-strain relation can be formulated as

$$\sigma_\alpha = C_{\alpha\beta}\,\epsilon_\beta \qquad (\alpha,\beta = 1,2,...,6)\,. \tag{2.4}$$

2.1.2 Seismic anisotropy

In general, anisotropy refers to the dependence of the stress-strain relation on direction. In seismics this mainly affects the velocities at which waves propagate through a medium. Contrary to that, the wave velocity and attenuation does not change with direction in isotropic media and the waves' polarization. The analysis of seismic anisotropy can, hence, allows to draw conclusions about the medium as it may provide information about the orientation of layers, fractures and minerals as well as the in-situ stress conditions Helbig and Thomsen (2005).

2.1.3 Observation & sources of seismic anisotropy

Seismic anisotropy can be observed in terms of directionally varying velocities in traveltime tomography, a change of the polarization vector and thus an actual change in particle motion by means of hodograms and most reliably by shear wave splitting Crampin (1984). The latter produces two shear waves with orthogonal polarization that arrive at different times and allow for the measurement of the traveltime difference δt, often called delay time.

Seismic anisotropy results from small-scale structures with a preferred orientation that find their expression on a larger scale (Thomsen, 1986). Small-scale hereby refers to a size smaller than the wavelength. In addition, the anisotropic subsurface feature has to have an extent of several wavelengths to cause effective anisotropy. Geologic features include fine layering in sedimentary rocks (Helbig, 1981, Thomsen, 1986), aligned fractures and cracks (Crampin, 1984, Gupta, 1973) or voids which might be filled with fluids (Nishizawa, 1982). Furthermore, a stress induced orientation of minerals or crystals such as in olivine and ice may result in anisotropic behavior of the propagating waves (Clayton, 2011). Moreover, the minerals itself might be anisotropic, which is then referred to as intrinsic anisotropy. Another source of anisotropy can be boreholes as they yield a concentration of stress by closing or opening cracks during drilling (Fang et al., 2013, Jaeger et al., 2007).

2.1.4 Symmetries

Typical anisotropic, geological structures exhibit some kind of transverse isotropy, where the medium behaves isotropic in the plane orthogonal to the axis of symmetry. Assuming transverse isotropic (TI) media (Thomsen, 1986), only five independent components of the stiffness tensor remain as there is no angular dependency of the wavefield parameters in one plane, which yields

$$C_{\mathrm{TI}} = \begin{pmatrix} c_{11} & c_{12} & c_{13} & 0 & 0 & 0 \\ c_{12} & c_{22} & c_{23} & 0 & 0 & 0 \\ c_{13} & c_{23} & c_{33} & 0 & 0 & 0 \\ 0 & 0 & 0 & c_{44} & 0 & 0 \\ 0 & 0 & 0 & 0 & c_{55} & 0 \\ 0 & 0 & 0 & 0 & 0 & c_{66} \end{pmatrix}. \tag{2.5}$$

Commonly investigated symmetries are vertically transverse isotropy (VTI), horizontally transverse isotropy (HTI) and tilted transverse isotropy (TTI). However, lower symmetries, like orthorhombic and monoclinic, can also be found in nature. While the first one consists of parallel vertical fractures that are embedded in a finely layered medium (Tsvankin, 2001) and can be described by a stiffness tensor with nine independent components, the latter has tilted fractures of at least two different orientations

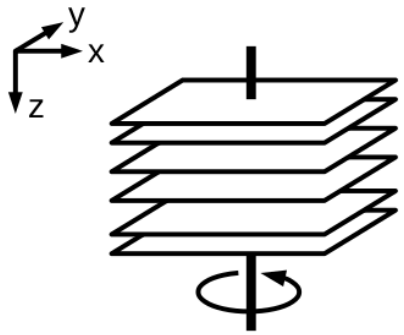

Figure 2.1: Schematic illustration of a VTI medium. The axis of symmetry is the z-axis that points vertically downwards. Within one layer the medium is isotropic.

with respect to the layers. This is expressed by a mirror symmetry of the stiffness tensor along one axis and 13 independent components (Ikelle and Amundsen, 2005). In the following, however, I will focus on the VTI case, where the axis of symmetry is vertical, and which provides a relatively simple model of an anisotropic medium. A sketch of such a VTI medium is shown in Figure 2.1. In a VTI medium the isotropic plane is the horizontal plane and the 3-axis is the vertical, hereafter referred to as z-direction, and thus the following relations between the stiffness tensor components can be identified:

$$c_{22} = c_{11} \tag{2.6}$$
$$c_{44} = c_{55} \tag{2.7}$$
$$c_{23} = c_{13} \tag{2.8}$$
$$c_{12} = c_{11} - 2\,c_{66} \tag{2.9}$$

This leads to the final form of the VTI stiffness tensor, with only five independent components, namely

$$C_{\mathrm{VTI}} = \begin{pmatrix} c_{11} & c_{11}-2\,c_{66} & c_{13} & 0 & 0 & 0 \\ c_{11}-2\,c_{66} & c_{11} & c_{13} & 0 & 0 & 0 \\ c_{13} & c_{13} & c_{33} & 0 & 0 & 0 \\ 0 & 0 & 0 & c_{55} & 0 & 0 \\ 0 & 0 & 0 & 0 & c_{55} & 0 \\ 0 & 0 & 0 & 0 & 0 & c_{66} \end{pmatrix}. \tag{2.10}$$

2.1.5 Vertically transverse isotropy (VTI)

For the case of weak anisotropy, i.e., less than 20%, of the VTI type, Thomsen (1986) derived equations for the angle-dependent phase velocities of P- and S-waves that are given by

$$v_{\mathrm{P}}(\theta) = v_{\mathrm{P0}}\left(1 + \delta \sin^2\theta\,\cos^2\theta + \varepsilon \sin^4\theta\right) \tag{2.11}$$
$$v_{\mathrm{SV}}(\theta) = v_{\mathrm{SV0}}\left(1 + \frac{v_{\mathrm{P0}}^2}{v_{\mathrm{SV0}}^2}(\varepsilon - \delta)\sin^2\theta\,\cos^2\theta\right) \tag{2.12}$$
$$v_{\mathrm{SH}}(\theta) = v_{\mathrm{SH0}}\left(1 + \gamma \sin^2\theta\right) \tag{2.13}$$

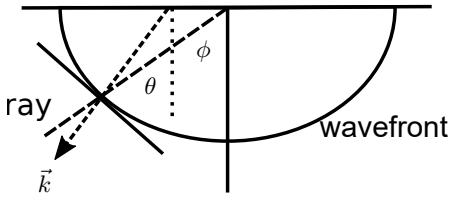

Figure 2.2: Definition of phase and group angle. The phase angle θ lies between the vertical and the wave vector $\vec{k}$, the group angle between the vertical and the ray (after Thomsen (1986)). Note that in case of the SV-wave the wavefront advances equally in vertical and horizontal direction, but faster or slower in between those two depending on the values of ε and δ. An increase of v_{SV} towards 45°, for instance, will produce a wavefront which approaches a quadratic shape.

with the index zero implying vertical velocities and where θ is the phase angle, which describes the angle between the vertical axis and the normal to the wavefront. Note that in the anisotropic case this angle differs from the group angle, which lies between the vertical axis and the direction of the ray (see Figure 2.2). The quantities ε, δ and γ are the so-called Thomsen parameters. Supplementary to ε being a measure of how much faster the P-wave propagates in the horizontal direction than the vertical, δ describes the change in the curvature of the wavefront, i.e., more precisely the moveout, near the vertical. They are defined as

$$\varepsilon = \frac{c_{11} - c_{33}}{2\,c_{33}} \tag{2.14}$$

$$\delta = \frac{(c_{13} + c_{55})^2 - (c_{13} - c_{55})^2}{2\,c_{33}(c_{33} - c_{55})} \tag{2.15}$$

in terms of elastic constants (see subsection 2.1.1). While ε is exact[1], δ is an approximation for weak anisotropy just as equations Equation 2.11 to Equation 2.13. Those two parameters only occur in the P/SV-case, i.e., the SH-wave is independent on them. Similarly to ε, γ is a measure for the SH-wave anisotropy, which can be calculated by

$$\gamma = \frac{c_{66} - c_{55}}{2\,c_{55}}\,. \tag{2.16}$$

Thomsen (1986) analyzes that, for small θ, the δ-term dominates the anisotropy of the P-wave, unless $\varepsilon \gg \delta$, such that iterative updates of the anisotropy parameters should be focused on δ in the P/SV-case. Moreover, the frequent assumption that $\varepsilon = \delta$, describing elliptical anisotropy, is rarely found in nature. Instead, ε and δ can even be of opposite sign, with δ becoming negative as a result of intrinsic anisotropy. In finely layered sedimentary rocks, δ is strictly smaller than ε according to Helbig (1979) and Berryman (1979). The values of the Thomsen parameters are usually all of the same order of magnitude of about 0 to 20 percent.

The behavior of the phase velocities as a function of the angle of incidence θ is presented in Figure 2.3. The vertical velocities and the Thomsen parameters are chosen based on average values of the tomography models that are introduced in subsection 3.4.2. The actual values are given in Table 2.1. It can be seen that the P-wave velocity shows a similar behavior as the SH-wave velocity. Their horizontal velocities

[1] An approximation for weak anisotropy, though, is given by Equation 2.96.

Table 2.1: Average parameter values of the anisotropic traveltime tomography models (see subsection 3.4.2).

Parameter	value
$v_{\mathrm{P,ver}}$ in m/s	1680
$v_{\mathrm{S,ver}}$ in m/s	272
ρ in kg/m^3	1984
ε	0.0052
δ	0.0011
γ	0.0334

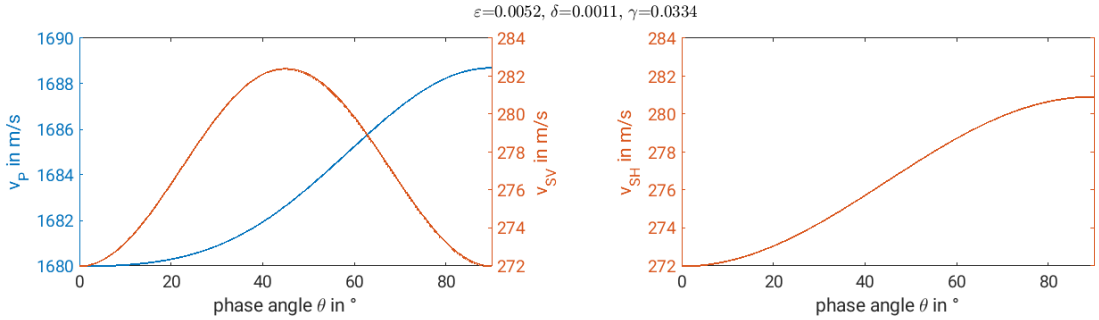

Figure 2.3: On the left-hand side the behavior of the P- and SV-wave velocities as a function of the angle of incidence are shown. The right-hand side depicts the angle-dependent velocity of the SH-wave. The curves are based on the average values of the Thomsen parameters ($\varepsilon = 0.0052, \delta = 0.0011$ and $\gamma = 0.0334$) that were obtained by the traveltime tomography by von Ketelhodt et al. (2019).

are higher than the vertical ones. Contrary to that, the horizontal SV-wave velocity is equal to the vertical velocity and instead has its maximum at about 45°. Note that if δ is bigger than ε the SV-wave velocity at 45° is smaller than the vertical one. This can, for instance, be the case in immature sandstone (Thomsen, 1986).

2.1.6 Elastic wave equations

In order to derive the elastic wave equations, I now consider the temporal derivative of Equation 2.2 assuming the elastic constants remain constant over time,

$$\dot{\sigma}_{ij} = C_{ijkl}\,\dot{\epsilon}_{kl} \tag{2.17}$$

with

$$\dot{\epsilon}_{kl} = \frac{1}{2}\left(\frac{\partial v_k}{\partial x_l} + \frac{\partial v_l}{\partial x_k}\right), \tag{2.18}$$

where v_i $(i = 1, 2, 3)$ are the particle velocity components. In addition to that, Newton's second law for infinitesimal deformation

$$\rho\,\dot{v}_i = \frac{\partial \sigma_{ij}}{\partial x_j} \tag{2.19}$$

with density ρ is required.
Since derivatives with respect to y vanish in a two dimensional space spanned by the

horizontal coordinate x and the depth z, the following system of first order partial differential equations is obtained:

P/SV-case

$$\rho\,\dot{v}_x = \frac{\partial \sigma_{xx}}{\partial x} + \frac{\partial \sigma_{xz}}{\partial z} \tag{2.20}$$

$$\rho\,\dot{v}_z = \frac{\partial \sigma_{xz}}{\partial x} + \frac{\partial \sigma_{zz}}{\partial z} \tag{2.21}$$

$$\dot{\sigma}_{xx} = c_{11}\,\frac{\partial v_x}{\partial x} + c_{13}\,\frac{\partial v_z}{\partial z} \tag{2.22}$$

$$\dot{\sigma}_{zz} = c_{13}\,\frac{\partial v_x}{\partial x} + c_{33}\,\frac{\partial v_z}{\partial z} \tag{2.23}$$

$$\dot{\sigma}_{xz} = c_{55}\left(\frac{\partial v_x}{\partial z} + \frac{\partial v_z}{\partial x}\right) \tag{2.24}$$

SH-case

$$\rho\,\dot{v}_y = \frac{\partial \sigma_{xy}}{\partial x} + \frac{\partial \sigma_{yz}}{\partial z} \tag{2.25}$$

$$\dot{\sigma}_{xy} = c_{66}\,\frac{\partial v_y}{\partial x} \tag{2.26}$$

$$\dot{\sigma}_{xy} = c_{55}\,\frac{\partial v_y}{\partial z} \tag{2.27}$$

This is the so-called stress-velocity formulation for the elastic VTI case. It can be seen that the P/SV-waves are fully decoupled from the SH-waves as the respective derivatives of the particle velocity and stress fields of the P/SV-case do not occur in the SH-case.

2.1.7 Viscoelastic equations

When seismic waves propagate through the earth they become attenuated due to geometrical spreading and scattering, but also because of intrinsic loss of energy that is transformed into heat. The energy loss is commonly described by the quality factor, also called Q-factor, that is defined as the inverse of the relative energy loss per cycle

$$Q = 2\pi\,\frac{E}{\Delta E}\,. \tag{2.28}$$

Its mathematical representation is given by

$$Q = \frac{\Re(C_{ijkl})}{\Im(C_{ijkl})} \tag{2.29}$$

as the quotient of the real and imaginary part of the complex modulus C_{ijkl}. In order to describe the processes in the rock phenomenologically (Liu et al., 1976) introduced the generalized standard linear solid (GSLS). The model describes absorption by a superposition of L relaxation mechanisms that are arranged in parallel and are composed of a Hooke body for the elastic behavior and a Newton body for absorption which are placed in series. The relaxation mechanism is characterized by the relaxation frequency f_l that allows to determine the relaxation time $\tau_{\sigma l} = {}^1\!/_{2\pi f_l}$ (Bohlen, 2002). Each relaxation process is then expressed according to Bai and Tsvankin (2016) in terms of the relaxation function

$$\Psi_{ij}(t) = C^R_{ijkl}\left(1 - \frac{1}{L}\sum_{l=1}^{L}\left(1 - \frac{\tau_{\varepsilon l}}{\tau_{\sigma l}}\right)e^{-t/\tau_{\sigma l}}\right)H(t)\,, \tag{2.30}$$

where C^R_{ijkl} is the relaxed elastic constant, $\tau_{\varepsilon l}$ the retardation time and $H(t)$ the Heaviside step function. The temporal derivative of Ψ can be interpreted as the impulse response of a viscoelastic medium such that the stress-strain relation can be formulated

in terms of a convolution of $\dot{\Psi}$ with the strain ε in the time domain The temporal derivative of Ψ can be interpreted as the impulse response of a viscoelastic medium such that the stress-strain relation can be formulated in terms of a convolution of $\dot{\Psi}$ with the strain ε in the time domain

$$\sigma_{ij}(t) = \dot{\Psi}_{ijkl}(t) * \varepsilon_{kl}(t)\,. \tag{2.31}$$

In order to avoid the convolution Carcione et al. (1988) and Robertsson et al. (1994) suggest to introduce so-called memory variables r which yields additional differential equations. The complete system of differential equations describing anisotropic, viscoelastic media is obtained by inserting the time derivative of the relaxation function into the time derivative of the viscoelastic stress-strain relation (Equation 2.31) which leads to

$$\dot{\sigma}_{ij} = C_{ijkl}\left(1 + \sum_{l=1}^{L}\left(\frac{\tau_{\varepsilon l}}{\tau_{\sigma l}} - 1\right)e^{-t/\tau_{\sigma l}}\right) v_{kl} - C_{ijkl}\sum_{l=1}^{L}\left(\frac{\tau_{\varepsilon l}}{\tau_{\sigma l}} - 1\right)e^{-t/\tau_{\sigma l}}\, H(t) * v_{kl}\,, \tag{2.32}$$

where it is used that $\dot{H}(t) = \delta(t)$, which picks the value of the strain at time zero, and $C^U_{ijkl} = C_{ijkl}(1 + \tau_{ijkl})$ as unrelaxed modulus.
The last term on the right hand side of the equation is then defined as the sum of memory variables. This yields the additional partial differential equations for the memory variables with

$$\dot{r}_{ij} = -\frac{1}{\tau_{\sigma l}}\left(C_{ijkl}\sum_{l=1}^{L}\left(\frac{\tau_{\varepsilon l}}{\tau_{\sigma l}} - 1\right) + r_{ij}\right)\,. \tag{2.33}$$

where $v_{k,l}$ denotes the derivative of the lth component of the particle velocity with respect to x_k. Finally, the viscoelastic equations for VTI media are given by

$$\rho\,\dot{v}_x = \frac{\partial \sigma_{xx}}{\partial x} + \frac{\partial \sigma_{xz}}{\partial z} \tag{2.34}$$

$$\rho\,\dot{v}_z = \frac{\partial \sigma_{xz}}{\partial x} + \frac{\partial \sigma_{zz}}{\partial z} \tag{2.35}$$

$$\dot{\sigma}_{xx} = c_{11}\,(1 + L\,\tau_{11})\,\frac{\partial v_x}{\partial x} + c_{13}\,(1 + L\,\tau_{13})\,\frac{\partial v_z}{\partial z} + r_{xx} \tag{2.36}$$

$$\dot{\sigma}_{zz} = c_{13}\,(1 + L\,\tau_{13})\,\frac{\partial v_x}{\partial x} + c_{33}\,(1 + L\,\tau_{33})\,\frac{\partial v_z}{\partial z} + r_{zz} \tag{2.37}$$

$$\dot{\sigma}_{xz} = c_{55}\,(1 + L\,\tau_{55})\left(\frac{\partial v_x}{\partial z} + \frac{\partial v_z}{\partial x}\right) + r_{xz} \tag{2.38}$$

$$\dot{r}_{xx} = -\frac{1}{\tau_\sigma}\left(c_{11}\,L\,\tau_{11}\,\frac{\partial v_x}{\partial x} + c_{13}\,L\,\tau_{13}\,\frac{\partial v_z}{\partial z} + r_{xx}\right) \tag{2.39}$$

$$\dot{r}_{zz} = -\frac{1}{\tau_\sigma}\left(c_{13}\,L\,\tau_{13}\,\frac{\partial v_x}{\partial x} + c_{33}\,L\,\tau_{33}\,\frac{\partial v_z}{\partial z} + r_{zz}\right) \tag{2.40}$$

$$\dot{r}_{xz} = -\frac{1}{\tau_\sigma}\left(c_{55}\,L\,\tau_{55}\left(\frac{\partial v_x}{\partial x} + \frac{\partial v_z}{\partial z}\right) + r_{xz}\right) \tag{2.41}$$

where Voigt's notation is applied once again. One can further define the dimensionless parameter τ as

$$\tau = \frac{\tau_{\varepsilon l}}{\tau_{\sigma l}} - 1 \tag{2.42}$$

that can be approximated by $\tau \approx 2/Q$ (Bai et al., 2017) for a constant Q-model. To calculate the τ_{13}, which is required to determine the unrelaxed modulus c_{13}, Q_{13} has to

be known. For isotropic attenuation Zhu and Tsvankin (2006) provide

$$Q_{13} = Q_{33} \frac{c_{33} - 2\,c_{55}}{c_{33} - 2\,c_{55}\frac{Q_{33}}{Q_{55}}}\,. \tag{2.43}$$

Further, using that $Q_{11} = Q_{33}$ in case of isotropic attenuation and applying the nomenclature $Q_{33} = Q_{\mathrm{P}}$ and $Q_{55} = Q_{\mathrm{S}}$, the viscoelastic constitutive equations with anisotropic velocities and isotropic attenuation are obtained.

2.2 Numerical implementation by finite differences

Apart from very simple models, the equations derived above cannot be solved analytically. Instead a numerical solver is required. Most commonly used are finite-difference (FD) and finite-element (FE) schemes. While the latter allow to account for topography, finite-differences tend to produce artificial scattering at non-flat surfaces. However, due to the settings, the acquisition geometry and the depth of interest of the field data, this will not have a negative impact in this work. By contrast, the advantages of the finite-difference method, like its relatively easy implementation and efficient calculation of gradients and wavefields, prevail.

2.2.1 Discretization

The space domain is discretized using a grid with equidistant grid points in both the horizontal direction x and the vertical direction z. In the following the grid point spacing is called Δh, such that the Cartesian coordinates (x, z) are given by $(i\,\Delta h, j\,\Delta h)$, where i and j are the respective grid point numbers. Similarly to the space domain, the time domain discretization uses a regular time sampling interval Δt to describe the time t by $t = n\,\Delta t$ with n being the n-th time step.

In order to avoid instabilities, while ensuring high accuracy, and decoupling of velocity and stress, a staggered grid as suggested by Virieux (1984, 1986) and Levander (1988) is chosen. Some variables are then no longer located at the same grid point, but shifted by half the distance between two adjacent grid points, $\Delta h/2$. The distribution of the variables and parameters in such a grid is shown in Figure 2.4. It can be seen that, on the one hand, the stress components are located at different positions, i.e., compressional stresses are located at the same, full grid point, shear stresses on a half-way between two grid points diagonal to that. The particle velocity components v_x and v_z are placed between two grid points in the horizontal and vertical direction, respectively. On the other hand, the model parameters represented by the density and the elastic constants are all located on full grid points.

The partial derivatives with respect to time and space, that occur in Equation 2.20 to Equation 2.27, are calculated by means of finite differences. In case of second-order central operators, only the neighboring grid points are used, such that the partial derivatives of a function f can be expressed by

$$\frac{\partial f}{\partial x}\,[n, i] \approx \frac{f\left[n, i + \frac{1}{2}\right] - f\left[n, i - \frac{1}{2}\right]}{\Delta h} \tag{2.44}$$

$$\frac{\partial f}{\partial t}\,[n, i] \approx \frac{f\left[n + \frac{1}{2}, i\right] - f\left[n - \frac{1}{2}, i\right]}{\Delta t}\,. \tag{2.45}$$

For higher orders in space, such as the sixth order that is used in this work, farther grid points have to be taken into account to compute the spatial derivatives. This approach

allows for a coarser spatial grid and hence a reduction of the number of grid points yielding less computational costs, while ensuring high accuracy. However, this also elongates the FD operator and weighting coefficients, here Holberg coefficients, have to be introduced to properly account for the contribution of the grid points that are taken into account.

Furthermore, the density ρ and some of the elastic constants have to be averaged in order to properly calculate the particle velocities and shear stresses. For the density this interpolation is given by the arithmetic average

$$\rho[j, i+\tfrac{1}{2}] = \frac{1}{2}\left(\rho[j,i] + \rho[j,i+1]\right) \tag{2.46}$$

$$\rho[j+\tfrac{1}{2}, i] = \frac{1}{2}\left(\rho[j,i] + \rho[j+1,i]\right) . \tag{2.47}$$

Contrary to that, the elastic constants have to be interpolated harmonically according to Moczo et al. (2004). Again, considering Figure 2.4 only c_{55} in the P/SV-case and c_{66} in the SH-case have to be averaged to accurately calculate σ_{xz} and σ_{xy}, respectively. The harmonic interpolation takes into account the four neighboring grid points and is thus given by[2]

$$c_{kk}[j+\tfrac{1}{2}, i+\tfrac{1}{2}] = \left(\frac{1}{4}\left(\frac{1}{c_{kk}}[j,i] + \frac{1}{c_{kk}}[j,i+1] + \frac{1}{c_{kk}}[j+1,i] + \frac{1}{c_{kk}}[j+1,i+1]\right)\right)^{-1} . \tag{2.48}$$

The final discretization of the elastic equations is shown below for Equation 2.20 using second order FD operators.

$$\begin{aligned} \rho[j, i+\tfrac{1}{2}] \frac{v_x^{n+\frac{1}{2}}[j, i+\tfrac{1}{2}] - v_x^{n-\frac{1}{2}}[j, i+\tfrac{1}{2}]}{\Delta t} \\ = \frac{\sigma_{xx}^n[j,i+1] - \sigma_{xx}^n[j,i]}{\Delta h} + \frac{\sigma_{xz}^n[j+\frac{1}{2}, i+\frac{1}{2}] - \sigma_{xz}^n[j-\frac{1}{2}, i+\frac{1}{2}]}{\Delta h} \end{aligned} \tag{2.49}$$

This equation can be rearranged such that the horizontal velocity of the future time step $v_x^{n+\frac{1}{2}}$ can be calculated based on the values of horizontal particle velocity and corresponding stresses of the current and past time steps.

$$\begin{aligned} v_x^{n+\frac{1}{2}}[j, i+\tfrac{1}{2}] = v_x^{n-\frac{1}{2}}[j, i+\tfrac{1}{2}] + \frac{1}{\rho\left[j, i+\frac{1}{2}\right]} \frac{\Delta t}{\Delta h} \left(\sigma_{xx}^n[j,i+1] - \sigma_{xx}^n[j,i]\right. \\ \left. + \sigma_{xz}^n[j+\tfrac{1}{2}, i+\tfrac{1}{2}] - \sigma_{xz}^n[j-\tfrac{1}{2}, i+\tfrac{1}{2}]\right) \end{aligned} \tag{2.50}$$

The remaining wave equations Equation 2.21 to Equation 2.24 can be treated in a similar manner obtaining FD schemes for future time steps of the particle velocity and stress field components.

2.2.2 Initial and boundary conditions

In order to obtain physically reasonable results, initial and boundary conditions must be applied. At time zero all particles in the medium are at rest and no stresses act on them. At the top boundary of the model a free surface condition has to be used that imitates the earth-air interface, where all stresses applied on a horizontal plane vanish

[2] Note that the double index of c_{kk} does *not* imply the Einstein summation convention, but refers to the diagonal components of the stiffness matrix.

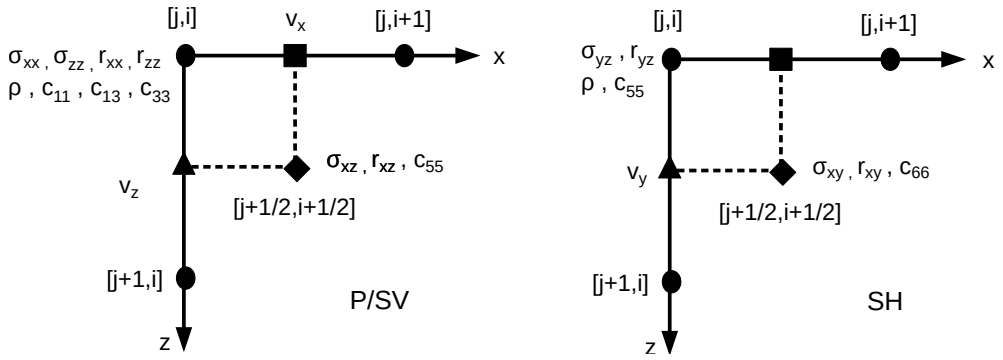

Figure 2.4: Distribution of the variables and parameters used in the FD modeling on a staggered grid following the descriptions by Virieux (1984, 1986). The illustration is adapted after Krampe (2018).

($\sigma_{xz} = \sigma_{yz} = \sigma_{zz} = 0$) at the surface location. The method which is implemented here is the so-called image or mirroring method (Levander, 1988). It works well for planar free surfaces and sets the stresses above the free surface to a value of opposite sign compared to those directly below it. To ensure stability, vertical derivatives of the velocities should not be used in the calculation of σ_{xx}. For this purpose, the condition $\sigma_{zz}|_{z=0} = 0$ is utilized (Levander, 1988). It yields the following alternative formulation of the vertical derivative of v_z (Krampe, 2018):

$$\begin{aligned} \sigma_{zz} &= \Delta t \left(c_{13} \frac{\partial v_x}{\partial x} + c_{33} \frac{\partial v_z}{\partial z} \right) = 0 \\ \Rightarrow \frac{\partial v_z}{\partial z} &= -\frac{c_{13}}{c_{33}} \frac{\partial v_x}{\partial x} \end{aligned}$$

The appropriate update of σ_{xx} is then given by

$$\sigma_{xx}^n = \sigma_{xx}^{n-1} + \Delta t \left(c_{11} - \frac{c_{13}^2}{c_{33}} \right) \frac{\partial v_x}{\partial x} \,. \tag{2.51}$$

Additionally to the free surface, absorbing boundaries are applied at the edges and bottom of the model to prevent artificial reflections at the numerical model boundaries. In this case a simple boundary conditions is implemented that damps the incoming waves exponentially instead of using a convolutional perfectly matching layer (CPML) (Komatitsch and Martin, 2007) as the latter might cause instabilities in the anisotropic case (Bécache et al., 2003).

2.2.3 Grid dispersion

Signal processing demands to have at least two samples per wavelength according to Nyquist's theorem. However, the finer the grid, the more accurate will be the solution. Computational cost considerations, though, suggest to limit the number of grid points. Hence, a compromise has to be found, in order to still avoid numerical dispersion related to spatial discretization, i.e., grid dispersion, while keeping the computational cost small. Therefore, the following condition can be formulated and must be fulfilled:

$$\Delta h \leq \frac{\lambda_{\min}}{n} = \frac{v_{\min}}{n\, f_{\max}} \,, \tag{2.52}$$

where $\lambda_{\min}$ is the minimal wavelength, n the grid points per wavelength, $v_{\min}$ the minimal velocity in the model and $f_{\max}$ the maximum frequency in the simulation. In practice, n is determined by the Holberg coefficients which ensure a minimal dispersion error of 0.1% at $3\,f_{\max}$ (Robertsson et al., 1994).

2.2.4 Numerical stability

Apart from the spatial discretization, the temporal discretization also influences the simulation. To ensure that the simulation stays stable the so-called Courant-Friedrichs-Lewy criterion (Courant et al., 1928, 1967) must be fulfilled, which is in the 2D case given by

$$\Delta t \leq \frac{\Delta h}{\gamma\sqrt{2}\,v_{\max}}\,, \tag{2.53}$$

where γ is the sum of weighting coefficients of the FD operator and $v_{\max}$ the maximum model velocity. The factor of $\sqrt{2}$ refers to a 2D simulation. A specific stability criterion for anisotropic FD simulations was derived by Pei et al. (2012) that considers the elastic constants. It is given by

$$\Delta t \leq \frac{1}{\gamma\sqrt{2}}\frac{\rho}{S} \tag{2.54}$$

with

$$S = \max\left\{\frac{c_{11}}{\Delta h^2}, \frac{c_{33}}{\Delta h^2}, \frac{c_{55}}{\Delta h^2}, \frac{c_{66}}{\Delta h^2}\right\}. \tag{2.55}$$

2.3 Full-waveform inversion

So far seismic wave propagation and its simulation was presented. Below I discuss how we can exploit this knowledge to deduce an image of the subsurface.

2.3.1 Inversion method

The objective of an inversion of seismic data is to obtain a model of the subsurface structure from the records of seismic waves that traveled through the medium. While traveltime tomography uses only the onset times of certain phases, full-waveform inversion (FWI) also considers the full waveform including the amplitudes. Thus, the models that are retrieved by FWI should not only explain the traveltimes, but the entire waveform. Unfortunately, this requires more computational resources, but promises a better image of the subsurface due to the higher information content that is used.

The idea of FWI was first introduced by Tarantola (1984), who used an acoustic approximation of the wave equation to describe the wavefield. He suggested to forward model synthetic data based on given initial subsurface models and compare it with field data. The difference between the two data sets is investigated by a correlation of the forward calculated wavefield at the source positions and the data residuals at the receiver positions which are propagated backward in time. The model parameters are updated in each iteration such that the misfit between the two wavefields is minimized. To ensure convergence, the initial models that are used for the forward simulation should not differ too much from the true models. More precisely, the waveforms should not be shifted by more than half a wavelength. Otherwise, cycle skipping is present which might cause the inversion to converge towards a local minimum.

The misfit between the observed and the simulated waveforms is defined by the objective function $J(m)$ which is often expressed by the L2 norm. During the inversion the misfit is reduced iteratively by slightly perturbing the model at each iteration by δm. Here, the model update is calculated using the steepest descent method and the new model at the current iteration is given by

$$m_{n+1} = m_n - \alpha_n P_n \left(\frac{\partial J}{\partial m}\right)_n , \tag{2.56}$$

where m_n is the model at the previous iteration, α_n the step length, P_n the preconditioning matrix and the last factor describes the gradient with respect to the model parameters. While the gradient defines the direction of the model update, the step length describes the size of the change. If the step size is chosen too big, the algorithm might not find the minimum, but actually overstep it. However, a step length too small might lead to a large number of iterations and hence a longer computation time. Therefore, a parabolic step length search proposed by Sourbier et al. (2009a,b), Brossier (2009) and Nocedal and Wright (1999) is applied to find an appropriate step length. To do so, the misfit at a few shots is calculated using different step lengths. The resulting misfit values are fitted by a parabolic curve. Its minimum represents the actual step length that will be used. In order to provide faster convergence the so-called preconditioned conjugate gradient method by Plessix and Mulder (2004) is applied, which uses the approximated Hessian as preconditioning factor. Further, the model perturbations also take into account the gradient of the previous iteration, such that the model update is given by

$$\delta m \to \delta m_c = \alpha_n \left(P_n \left(\frac{\partial J}{\partial m}\right)_n + \beta_n \, \delta m_{n-1}\right) . \tag{2.57}$$

The weighting factor β_n can be defined in different ways. Here, the definition by Polak and Ribiere (1969) is chosen, which is given by

$$\beta_n = \frac{\nabla J_n^T (\nabla J_n - \nabla J_{n-1})}{\nabla J_{n-1}^T \, \nabla J_{n-1}} . \tag{2.58}$$

It considers the difference between the current and the previous model perturbation, normalized by the previous one. According to Nocedal and Wright (1999) and Liu et al. (2017), this definition of the weighting factor is more robust and efficient than the one by Fletcher (1964), for instance.

2.3.2 Gradient calculation

As discussed above, updating the models requires to know the gradients of the objective function J. Those can be calculated using Lagrangian multipliers, which is a method that allows to solve optimization problems while taking into account given constraints. Following the description of Plessix (2006) and Liu and Tromp (2006) as well as the derivation by Krampe (2018) for the SH-case, I deduce the gradients for the VTI P/SV-case hereafter.

As mentioned above, the goal of FWI is to minimize the objective function, which is often chosen as the L2 norm

$$J(m) = \frac{1}{2} \sum_r \sum_i \int_0^T \mathrm{d}t \, (v_i - v_{obs,i})^2 , \tag{2.59}$$

where v_i are the components of the forward simulated particle velocities, $v_{obs,i}$ the observed ones and the sum over r indicates the summation over all receivers. Further, the stress-velocity formulation of the elastic equations with external force density f_i

$$\rho\,\dot{v}_i = \frac{\partial \sigma_{ij}}{\partial x_j} + f_i \tag{2.60}$$

$$\dot{\sigma}_{ij} = C_{ijkl}\,\frac{\partial v_k}{\partial x_l} \tag{2.61}$$

pose as the constraints as well as the initial conditions $v_i(t=0)=0$ and $\sigma_{ij}(t=0)=0$ as stated in section 2.2. This allows to formulate the augmented Lagrangian $\mathcal{L}$ with the Lagrangian multipliers $\psi_i^{(1)}$ and $\psi_{ij}^{(2)}$ following the nomenclature of Krampe (2018) as

$$\begin{aligned}\mathcal{L} = \frac{1}{2}\sum_r\sum_i\int_0^T \mathrm{d}t\,(v_i - v_{obs,i})^2 &- \iint \mathrm{d}\Omega\,\mathrm{d}t\,\psi_i^{(1)}\left(\rho\,\dot{v}_i - \frac{\partial\sigma_{ij}}{\partial x_j} - f_i\right)\\ &- \iint \mathrm{d}\Omega\,\mathrm{d}t\,\psi_{ij}^{(2)}\left(\dot{\sigma}_{ij} - C_{ijkl}\,\frac{\partial v_k}{\partial x_l}\right),\end{aligned} \tag{2.62}$$

where $\mathrm{d}\Omega$ denotes an integration over the entire volume.

In order to optimize this problem, the derivatives with respect to the parameters particle velocity v_i and stress components σ_{ij} as well as the Lagrangian multipliers $\psi_i^{(1)}$ and $\psi_{ij}^{(2)}$ have to be determined and set to zero. Since the parameters v_i and σ_{ij} are not directly available in Equation 2.62, but only their temporal and spatial derivatives, an integration by parts in time and space is applied to recover them. This yields

$$\begin{aligned}\mathcal{L} = \frac{1}{2}\sum_r\sum_i\int_0^T \mathrm{d}t\,(v_i - v_{obs,i})^2 &+ \iint \mathrm{d}\Omega\,\mathrm{d}t\left(\rho\,\dot{\psi}_i^{(1)}v_i - \frac{\partial\psi_i^{(1)}}{\partial x_j}\sigma_{ij} + \dot{\psi}_i^{(1)}f_i\right)\\ &+ \iint \mathrm{d}\Omega\,\mathrm{d}t\left(\dot{\psi}_{ij}^{(2)}\sigma_{ij} - \frac{\partial(\psi_{ij}^{(2)}\,C_{ijkl})}{\partial x_l}\,v_k\right).\end{aligned} \tag{2.63}$$

The terms that have to be evaluated at the boundaries in the integration by parts become zero. However, they still contain information by providing boundary conditions for the Lagrangian multipliers that are given by

$$\psi_i^{(1)}(T) = 0 \tag{2.64}$$

$$\psi_{ij}^{(2)}(T) = 0\,. \tag{2.65}$$

Eventually, the required derivatives can be calculated and yield

$$\frac{\partial\mathcal{L}}{\partial v_i} = 0 \quad\Leftrightarrow\quad \rho\,\dot{\psi}_i^{(1)} = \frac{\partial(\psi_{kl}^{(2)}\,c_{klij})}{\partial x_j} - (v_i - v_{obs,i})\,, \tag{2.66}$$

$$\frac{\partial\mathcal{L}}{\partial \sigma_{ij}} = 0 \quad\Leftrightarrow\quad \dot{\psi}_{ij}^{(2)} = \frac{\partial\psi_i^{(1)}}{\partial x_j}\,. \tag{2.67}$$

Comparing those equations with Equation 2.60 and Equation 2.61 reveals that they have the same structure. However, the boundaries are now given at $t=T$ (see Equation 2.64). This can be handled by replacing t by $T-t$, which effectively reverses time. Further, we can substitute $T-t$ by τ and use $\dot{\psi}_i^{(1)}(T-t) = -\dot{\psi}_i^{(1)}$ which leads to

$$\rho\,\dot{\psi}_i^{(1)}(\tau) = -\frac{\partial(\psi_{kl}^{(2)}(\tau)\,c_{klij})}{\partial x_j} + (v_i - v_{obs,i})\,, \tag{2.68}$$

$$\dot{\psi}_{ij}^{(2)}(\tau) = -\frac{\partial \psi_i^{(1)}(\tau)}{\partial x_j}\,. \tag{2.69}$$

with the boundary conditions $\psi_i^{(1)}(\tau = 0) = 0$ and $\psi_{ij}^{(2)}(\tau = 0) = 0$. To obtain the same structure for these equations as the wave equations, $-\psi_{kl}^{(2)}(\tau)\, c_{klij}$ is placed by $\tilde{\psi}_{ij}^{(2)}$. The resulting equations

$$\rho\, \dot{\psi}_i^{(1)}(\tau) = \frac{\partial \tilde{\psi}_{ij}^{(2)}}{\partial x_j} + (v_i - v_{obs,i})\,, \tag{2.70}$$

$$\dot{\tilde{\psi}}_{ij}^{(2)}(\tau) = C_{ijkl} \frac{\partial \psi_k^{(1)}(\tau)}{\partial x_l} \tag{2.71}$$

are the so-called adjoint equations with the adjoint wavefields $\psi_i^{(1)}$ and $\tilde{\psi}_{ij}^{(2)}$. The latter are calculated by the back propagation of the adjoint source, which is defined as the residual between the observed and the forward calculated traces. Thus, $\psi_i^{(1)}$ can be considered as the back propagated particle velocity field, from now on denoted as $v_i^\star$, and $\tilde{\psi}_{ij}^{(2)}$ as the back propagated stress field called $\sigma_{ij}^\star$.

Since the derivatives with respect to the model parameters of the objective function are the same as those of the augmented Lagrangian, the gradients are given by

$$\frac{\partial J}{\partial \rho} = -\int \mathrm{d}t\, v_i^\star\, \dot{v}_i \tag{2.72}$$

$$\frac{\partial J}{\partial C_{ijkl}} = \int \mathrm{d}t\, \psi_{ij}^{(2)}\, \frac{\partial v_k}{\partial x_l}\,. \tag{2.73}$$

To be able to express the gradient with respect to the elastic constants in terms of the back-propagated stress field, one must invert the stiffness matrix. For the P/SV-case I first rewrite Equation 2.22 to Equation 2.24 in matrix notation

$$\begin{pmatrix} \dot{\sigma}_{xx} \\ \dot{\sigma}_{zz} \\ \dot{\sigma}_{xz} \end{pmatrix} = \begin{pmatrix} c_{11} & c_{13} & 0 \\ c_{13} & c_{33} & 0 \\ 0 & 0 & c_{55} \end{pmatrix} \cdot \begin{pmatrix} v_{x,x} \\ v_{z,z} \\ v_{x,z} + v_{z,x} \end{pmatrix} \tag{2.74}$$

with $v_{x,z}$ being the partial derivative of v_x with respect to z and so on. Then the system of equations is solved for the required partial derivatives of the particle velocity components, yielding

$$\begin{pmatrix} v_{x,x} \\ v_{z,z} \\ v_{x,z} + v_{z,x} \end{pmatrix} = \begin{pmatrix} \frac{c_{33}}{c_{11}c_{33} - c_{13}^2} & -\frac{c_{13}}{c_{11}c_{33} - c_{13}^2} & 0 \\ -\frac{c_{13}}{c_{11}c_{33} - c_{13}^2} & \frac{c_{11}}{c_{11}c_{33} - c_{13}^2} & 0 \\ 0 & 0 & \frac{1}{c_{55}} \end{pmatrix} \cdot \begin{pmatrix} \dot{\sigma}_{xx} \\ \dot{\sigma}_{zz} \\ \dot{\sigma}_{xz} \end{pmatrix}\,. \tag{2.75}$$

Thus, Equation 2.73 can be rewritten in terms of the adjoint wavefields as

$$\frac{\partial J}{\partial C_{ijkl}} = \int \mathrm{d}t\, \left(-[C_{\mathrm{VTI}}^{-1}]_{ijkl}\, \sigma_{ij}^\star\right)\, \left([C_{\mathrm{VTI}}^{-1}]_{ijkl}\, \dot{\sigma}_{ij}\right)\,. \tag{2.76}$$

Consequently, the final gradients for the P/SV-case are given by

$$\frac{\partial J}{\partial c_{11}} = -\int \mathrm{d}t\, [\tilde{c}_{11}^2 \sigma_{xx}^\star \dot{\sigma}_{xx} + \tilde{c}_{13}^2 \sigma_{zz}^\star \dot{\sigma}_{zz} + \tilde{c}_{11}\tilde{c}_{13}(\sigma_{xx}^\star \dot{\sigma}_{zz} + \sigma_{zz}^\star \dot{\sigma}_{xx})]\,, \tag{2.77}$$

$$\frac{\partial J}{\partial c_{33}} = -\int \mathrm{d}t\, [\tilde{c}_{13}^2 \sigma_{xx}^\star \dot{\sigma}_{xx} + \tilde{c}_{33}^2 \sigma_{zz}^\star \dot{\sigma}_{zz} + \tilde{c}_{13}\tilde{c}_{33}(\sigma_{xx}^\star \dot{\sigma}_{zz} + \sigma_{zz}^\star \dot{\sigma}_{xx})]\,, \tag{2.78}$$

$$\frac{\partial J}{\partial c_{13}} = -\int \mathrm{d}t \,[(\tilde{c}_{11}\tilde{c}_{13} + \tilde{c}_{13}^2)\sigma_{xx}^{\star}\dot{\sigma}_{xx} + (\tilde{c}_{11}\tilde{c}_{33} + \tilde{c}_{13}\tilde{c}_{33})\sigma_{xx}^{\star}\dot{\sigma}_{zz} + (\tilde{c}_{13}^2 + \tilde{c}_{33}\tilde{c}_{13})\sigma_{zz}^{\star}\dot{\sigma}_{xx} + (\tilde{c}_{13}\tilde{c}_{33} + \tilde{c}_{33}^2)\sigma_{zz}^{\star}\dot{\sigma}_{zz} + \tilde{c}_{55}\sigma_{xz}^{\star}(\tilde{c}_{13}\dot{\sigma}_{xx} + \tilde{c}_{33}\dot{\sigma}_{zz})]\,, \tag{2.79}$$

$$\frac{\partial J}{\partial c_{55}} = -\int \mathrm{d}t\, \tilde{c}_{55}^2 \sigma_{xz}^{\star}\dot{\sigma}_{xz} \tag{2.80}$$

with

$$\tilde{c}_{11} = \frac{c_{33}}{c_{11}c_{33} - c_{13}^2}\,, \tag{2.81}$$

$$\tilde{c}_{13} = -\frac{c_{13}}{c_{11}c_{33} - c_{13}^2}\,, \tag{2.82}$$

$$\tilde{c}_{33} = \frac{c_{11}}{c_{11}c_{33} - c_{13}^2}\,, \tag{2.83}$$

$$\tilde{c}_{55} = \frac{1}{c_{55}}\,. \tag{2.84}$$

For the gradient with respect to c_{55} I once again exploit the symmetry of the stiffness tensor in TI media, where $c_{31} = c_{13}$, as well as the symmetry of the stress tensor, such that we can deduce that $\psi_{31}^{(2)} = \psi_{13}^{(2)}$. Knowing this, we rewrite $\psi_{13}^{(2)} \frac{\partial v_x}{\partial z}$ as $\frac{1}{2}(\psi_{13}^{(2)} \frac{\partial v_x}{\partial z} + \psi_{31}^{(2)} \frac{\partial v_z}{\partial x}) = \frac{1}{2}\psi_{13}^{(2)} (\frac{\partial v_x}{\partial z} + \frac{\partial v_z}{\partial x})$ and thus are able to properly use the last line of the system of equations in Equation 2.74.

2.3.3 Parameterization

The gradients with respect to the elastic constants allow to introduce other possible parameterizations, for instance in terms of $(\rho, v_\mathrm{P}, v_\mathrm{SV}, \varepsilon, \delta)$ or $(\rho, v_\mathrm{P}, v_\mathrm{SV}, v_\mathrm{P,hor}, v_\mathrm{SV,hor})$. The latter encompasses parameters that are all in a similar order of magnitude which is beneficial regarding fast convergence and stability according to Köhn et al. (2012) who showed this for parameters used in the isotropic, elastic case. Though the use of vertical and horizontal velocities together with the density ρ would present the most intuitive representation, using the horizontal SV-wave velocity $v_\mathrm{SV,hor}$ might cause problems, because it is supposed to be equal to the vertical SV-wave velocity (see subsection 2.1.5), which is a criterion that is hard to fulfill in the inversion. Therefore, we choose the SV-wave velocity at an incidence angle of 45° instead, which is given by

$$v_\mathrm{SV}(45°) = v_\mathrm{SV}\left(1 + \frac{v_\mathrm{P}^2}{v_\mathrm{SV}^2}\frac{\varepsilon - \delta}{4}\right) \tag{2.85}$$

in the case of weak anisotropy according to Thomsen (1986) (see also Equation 2.12).

For the derivation of the gradients with respect to $(\rho, v_\mathrm{P}, v_\mathrm{SV}, v_\mathrm{P,hor}, v_\mathrm{SV}(45°))$, we use Thomsen's relations between the elastic constants and the velocities

$$c_{11} = \rho\, v_\mathrm{P,hor}^2\,, \tag{2.86}$$

$$c_{33} = \rho\, v_\mathrm{P}^2\,, \tag{2.87}$$

$$c_{55} = \rho\, v_\mathrm{SV}^2\,, \tag{2.88}$$

$$c_{13} = \rho\left(\sqrt{2\,\delta\, v_\mathrm{P}^2\,(v_\mathrm{P}^2 - v_\mathrm{SV}^2) + (v_\mathrm{P}^2 - v_\mathrm{SV}^2)^2} - v_\mathrm{SV}^2\right)\,, \tag{2.89}$$

where I solve Equation 2.15 for c_{13} and insert c_{33} and c_{55} to obtain Equation 2.89. Thus, also using the chain rule together with the equations Equation 2.86 to Equation 2.89 and Equation 2.85, the gradients with respect to the chosen parameters are

$$\frac{\partial J}{\partial v_{\mathrm{P}}} = \frac{\partial J}{\partial c_{33}} 2\,\rho\,v_{\mathrm{P}}\,, \tag{2.90}$$

$$\frac{\partial J}{\partial v_{\mathrm{P,hor}}} = \frac{\partial J}{\partial c_{11}} 2\,\rho\,v_{\mathrm{P,\,hor}}\,, \tag{2.91}$$

$$\frac{\partial J}{\partial v_{\mathrm{SV}}} = \frac{\partial J}{\partial c_{55}} 2\,\rho\,v_{\mathrm{SV}}\,, \tag{2.92}$$

$$\begin{aligned}\frac{\partial J}{\partial v_{\mathrm{SV}}(45°)} = {} & \frac{\partial J}{\partial c_{11}} 8\,\rho\,v_{\mathrm{P,\,hor}}\,\frac{v_{\mathrm{SV}}}{v_{\mathrm{P}}} \\ & + \frac{\partial J}{\partial c_{33}}\,\rho\,v_{\mathrm{SV}} \left(\frac{\left(\frac{v_{\mathrm{P,hor}}}{v_{\mathrm{P}}} - 1\right) - \delta}{4}\right)^{-1} \\ & + \frac{\partial J}{\partial c_{55}} 2\,\rho\,v_{\mathrm{SV}} \left(1 - \frac{v_{\mathrm{P}}^2}{v_{\mathrm{SV}}^2}\frac{\left(\frac{v_{\mathrm{P,hor}}}{v_{\mathrm{P}}} - 1\right) - \delta}{4}\right)^{-1} \\ & + \frac{\partial J}{\partial c_{13}} \left(-\frac{4\,\rho\,v_{\mathrm{SV}}\,(v_{\mathrm{P}}^2 - v_{\mathrm{SV}}^2)}{\sqrt{2\,\delta\,(v_{\mathrm{P}}^2 - v_{\mathrm{SV}}^2)\,v_{\mathrm{P}}^2 + (v_{\mathrm{P}}^2 - v_{\mathrm{SV}}^2)^2}}\right)\end{aligned} \tag{2.93}$$

$$\begin{aligned}\frac{\partial J}{\partial \rho'} = {} & \frac{\partial J}{\partial c_{33}}\,v_{\mathrm{P}}^2 + \frac{\partial J}{\partial c_{11}}\,v_{\mathrm{P,\,hor}}^2 + \frac{\partial J}{\partial c_{55}}\,v_{\mathrm{SV}}^2 \\ & + \frac{\partial J}{\partial c_{13}} \left(\sqrt{2\,\delta\,(v_{\mathrm{P}}^2 - v_{\mathrm{SV}}^2)\,v_{\mathrm{P}}^2 + (v_{\mathrm{P}}^2 - v_{\mathrm{SV}}^2)^2} - v_{\mathrm{SV}}^2\right) + \frac{\partial J}{\partial \rho}\end{aligned} \tag{2.94}$$

with

$$\delta = \frac{1}{v_{\mathrm{P}}^2}\left(\frac{v_{\mathrm{P,\,hor}}^2}{2} - 4\,v_{\mathrm{SV}}\,v_{\mathrm{SV}}(45°) + 4\,v_{\mathrm{SV}}^2\right) - \frac{1}{2}\,. \tag{2.95}$$

Due to the change in parameterization, the gradient regarding the density ρ is altered and referred to as ρ'. For the gradient with respect to $v_{\mathrm{SV}}(45°)$ and ρ', I additionally use the assumption of weak anisotropy, such that the horizontal P-wave velocity can be expressed by

$$v_{\mathrm{P,hor}} = v_{\mathrm{P}}\,(1 + \varepsilon)\,. \tag{2.96}$$

Hence, this gradient formulation is only valid for VTI media that merely exhibit weak anisotropy and cannot be transferred to the isotropic case.

3. Field data and traveltime tomography

3.1 Setting

3.1.1 Safira research test site

The Safira research test site is located about 40 km south of Leipzig and 5 km east of Zeitz in eastern Germany (Dietze, 2007).[3] Geologically, it is situated at the southern border of the Elster sedimentary basin, where Tertiary and Quaternary sedimentary deposits of the Weiße Elster can be found that dip to North and Northeast. At the site, there are two aquifers made of medium to coarse-grained sand which are separated by layered clay and interbedded lignite seams (von Ketelhodt et al., 2019). During the glacial period of the Elster-Saale the clay and lignite became over-consolidated at an extent of about 15 m of thickness. Consolidation means that the soil gradually changed its volume due to a change in pressure. An over-consolidated layer therefore refers to a condition of the rock in which the current effective stress exerted by the overburden is smaller than the one experienced in the past. When the region was covered by an ice shield, the soil got consolidated due to the pressure that was applied by the ice. As the ice melted the pressure decreased faster than the earth could react and compensate the change in pressure. Furthermore, the layers below the first aquifer are saturated such that refraction effects are limited (von Ketelhodt et al., 2018). All in all, such a geological setting with horizontal layering that experienced a change of stress conditions is expected to show VTI anisotropy.

3.1.2 Data acquisition

Geometry

The data were acquired by von Ketelhodt et al. (2019) in two boreholes with a distance of 13.45 m between them. The orientation of the borehole plane is approximately NNE-SSW. The inclination of the boreholes is less than 0.5 m over the entire depth range of 50 m. The diameter of the boreholes varies with depth from 32.4 cm down to 24 m depth and 27.3 cm down to 54 m depth. The casing is a PEHD-pipe, which is penetrable below 34 m depth. The water table is located in about 9.6 m depth. Logging data provides information about gravel in the upper part, clay in intermediate depths and lignite and gravel in the lower part of the borehole. Three-component receivers were placed in depths from 5 to 49 m with a spacing of 1 m. However, we will focus on shot depth of 10 to 30 m and receiver depths of 10 to 29 m, since that is the depth range where anisotropy

[3] A map of the site and the locations of the boreholes B29 and B59 can be found in von Ketelhodt et al. (2018) Figure 1.

Table 3.1: Acquisition parameters

parameter	value
source x-coordinate	13.45 m
source depths	$10 - 30$ m
source spacing	1 m
main frequency	110 Hz
receiver x-coordinate	0 m
receiver depths	$10 - 29$ m
receiver spacing	1 m
natural sensor frequency	10 Hz
sampling rate dt	$\frac{1}{2^{14}}$ s
recording time T	0.5 s
delay time t_d	60 ms

is expected and for which an anisotropic traveltime tomography was performed by von Ketelhodt et al. (2019). The transmission geometry allows for a dense ray coverage of the subsurface between the two boreholes. A sketch of the acquisition geometry and the ray coverage by straight rays, where a homogeneous models is assumed, is shown in Figure 3.1.

Sources & receivers

The sources and receivers are developed and produced by the company *Geotomographie GmbH* in Neuwied. The three-component receivers, one vertical component and two horizontal ones, can be oriented from the surface using stiff hoses which prevent torsion of the receiver spreads, and an attached magnetic compass. The latter enable an orientation of the receiver spreads with a deviation of $\pm 2.5°$. Both the receivers and the sources are pneumatically clamped to the borehole walls. The sources can produce signals with up to 4 kHz depending on the geology and borehole distance (Geotomographie GmbH, 2021).

Shots were fired twice (up-hole and down-hole) at each designated position using a prototype of a source that predominantly generates vertically polarized S-waves, hereafter referred to as SV-waves. Additionally, an SH-wave source was used that stroke perpendicular to the borehole plane. However, here, we will only model SV-source data because we are interested in the PSV-VTI-case.
The receivers are oriented such that their Z-component points downwards and their X-component is oriented in the direction of the borehole plane. The Y-component is orthogonal to the other two components by construction. Note that due to the slight inclination of the borehole and deviation from the ideal borehole plane as well as the way the geophones are oriented from the surface, though to a lesser extent, the actual receiver positions differ from the planned ones and the geophone components themselves are not properly aligned with the defined coordinate system (see also section 3.4).

A summary of the acquisition parameters can be found in Table 3.1.

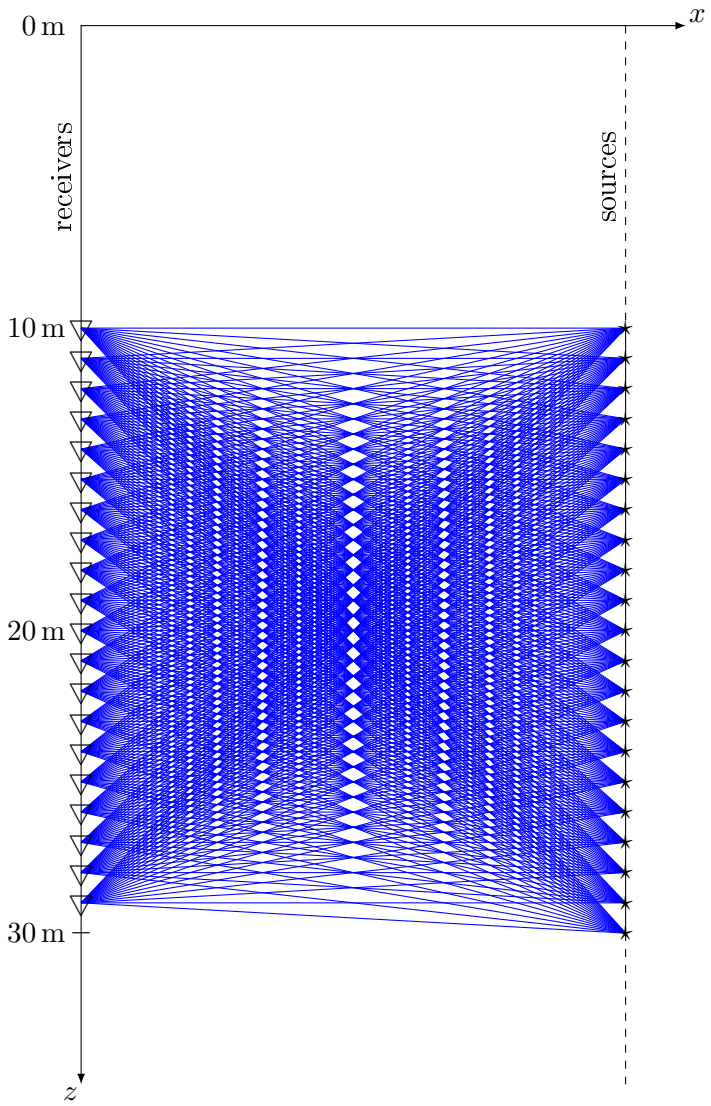

Figure 3.1: Acquisition geometry and ray coverage. $\triangledown$ marks receiver positions, $\star$ source positions. The ray coverage (blue) is based on the assumption of a homogeneous medium, where rays are straight lines.

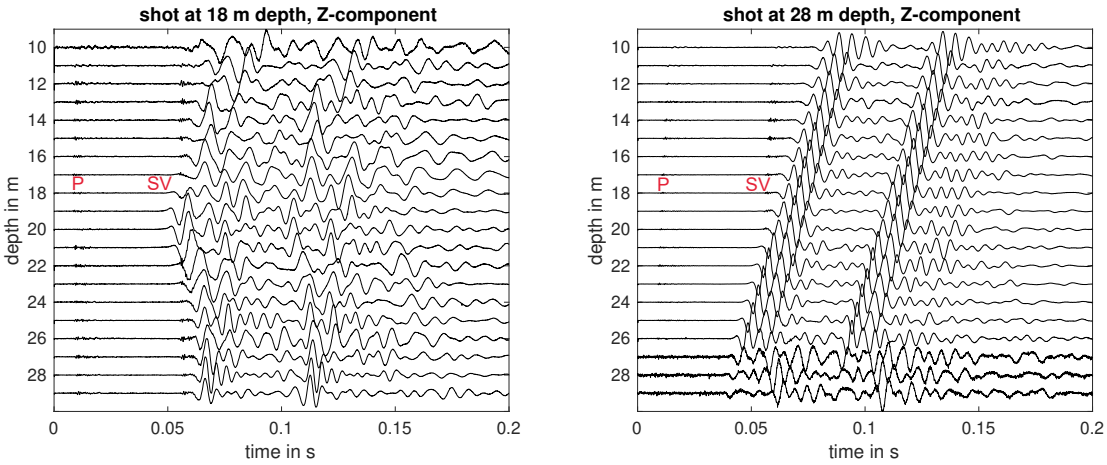

Figure 3.2: Shot gather for a source at 18 m (left) and 28 m depth (right). Receivers are located in depths of 10 to 29 m. Depicted is the Z-components, on which the SV-waves are predominantly registered.

3.2 Data quality

3.2.1 Shot gathers

In order to assess the data quality, all shot gathers are inspected visually. Figure 3.2 (left) shows the shot gather for the a shot at 18 m depth, i.e., in this project intermediate depth, recorded at the Z-component, where we predominantly expect to observe SV-waves. The small amplitude P-waves can be seen at onset times between 7 and 9 ms, though they almost get lost in the noise which can be observed on top of the waveforms. The SV-waves arrive between 47 ms and 57 ms. Before the S-wave onset one can also observe some ringing, which could be caused by parasitic resonances of the geophones.

Borehole-specific events such as tube waves cannot be identified in the shot gather on the left hand side at the considered receivers. This is not surprising regarding the considered depth range as they are significantly weaker in air-filled boreholes than in fluid-filled ones, where they can be observed as high-amplitude linear events that form a triangle when the shot is located centrally relative to the receiver spread (Mari and Vergniault, 2020).

Some shot gathers with a deeper shot position tend to be more noisy at the deep receivers, while the shallower depict cleaner waveforms. An example is shown in Figure 3.2 (right). A reason might be the reduced diameter of the boreholes. The linear event in the shot gather on the right hand side could be interpreted as tube waves at first sight. A closer look on the waveforms, though, reveals that they are very similar to the first arrivals. Hence, it is suspected that the this linear event with high amplitudes is caused by malfunctioning of the source.

3.2.2 Amplitude spectra

In order to study the frequency content of the data the average amplitude spectrum over all shots and traces is calculated. It is shown in Figure 3.3. The frequencies dominating the recordings range from about 30 Hz to 250 Hz with a coherently large peak around 110 Hz.

The notches in the spectrum appearing every 15 to 20 Hz are probably related to the

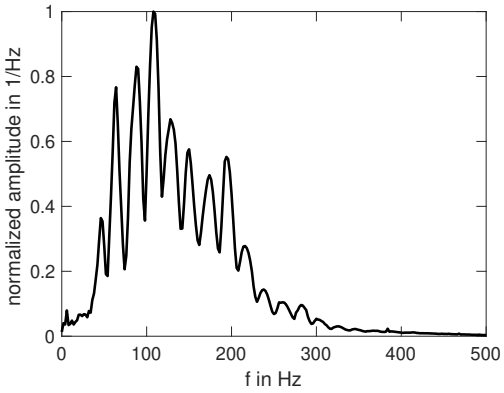

Figure 3.3: Average amplitude spectrum of all shots and traces. The data is dominated by frequencies between about 30 and 250 Hz with a maximum peak at 110 Hz.

source signature, which is unknown. Apart from that, the impedance discontinuity between the borehole and the medium can act as a secondary source generating events that are comparable to ghosts in their appearance in the spectrum.

3.3 Traveltime tomography

In previous studies von Ketelhodt et al. (2018, 2019) used the presented crosshole data to obtain an image of the subsurface by means of traveltime tomography. Their objective was to study the S-wave velocity change with increased stress and eventually derive more reliable lithologic and geotechnical parameters by taking into account the detected anisotropy.
For this purpose they performed two kinds of traveltime tomographies, an isotropic separate inversion and an anisotropic joint inversion, where both the data generated with the SV-source and the SH-source were used. The isotropic separate inversion shows that there seems to be a horizontally layered medium. Moreover, the P- and S-wave velocity distribution differs and the S-wave velocities correlate less with the borehole logs than the P-wave velocities. Furthermore, X-shaped distortions are observed in the S-wave velocity models. This indicates that anisotropy might be present in form of a VTI medium. A polarization analysis confirms the presence of anisotropy (von Ketelhodt et al., 2019). Hence, taking VTI anisotropy into account, one would expect to obtain better models of the subsurface.

3.3.1 Separate inversion procedure for isotropic models

A separate inversion of the picked P, SV and SH traveltimes allows to retrieve isotropic models. Von Ketelhodt et al. (2019) use homogeneous starting models that are determined based on the average velocities of all straight ray paths. Then the horizontal rays are used in a straight-ray inversion solving the inversion problem in the least-squares sense. Thereby the traveltime residuals $\delta\tau$ are defined after Zhou et al. (2008) in terms of a first order traveltime perturbation equation given by

$$\delta\tau = \int_R (\delta\vec{p} \cdot \mathrm{d}\vec{x} - \mathrm{d}\vec{p} \cdot \delta\vec{x}) \tag{3.1}$$

where $\vec{p}$ is the slowness vector and $\vec{x}$ a location vector. Additionally, a Tikhonov regularization is applied which suppresses noise resulting from picking inaccuracies and has

a smoothing effect by the use of the Laplacian operator that acts as a low-pass filter. The least-squares QR-factorization (LSQR) method (Paige and Saunders, 1982), which is a conjugate-gradient method, is chosen to iteratively update the slowness model until the models differ 1% maximum. At this point the Jacobian is recalculated. Afterwards a curved-ray tracing algorithm by Giroux and Gloaguen (2012) is applied ten times.

3.3.2 Joint inversion procedure for anisotropic models

In the joint inversion of the SV- and SH-source data von Ketelhodt et al. (2018, 2019) add cross-gradient constraints proposed by Gallardo and Meju (2003, 2004) to ensure structural similarity. Using the isotropic models as starting models together with estimates of the anisotropy parameters from borehole logs, the curved-ray tracing algorithm, that was developed further for VTI media by von Ketelhodt et al. (2018), is run with ten iterations. After each of those iterations 25 LSQR iterations are performed and the model parameters' values are limited separately. For a joint inversion the LSQR method is extended by the cross-gradient constraint expressed as

$$\vec{t}_k = \nabla \vec{m}_k^{(1)} \times \nabla \vec{m}_k^{(2)} \stackrel{!}{=} \vec{0}\,, \tag{3.2}$$

which ensures the coupling of the parameters. As the problem is a 2D problem the only non-zero component of the cross-gradient function $\vec{t}_k$ is the y-component. It is discretized by a forward difference scheme (Gallardo and Meju, 2004, von Ketelhodt et al., 2018) and approximated by a first-order Taylor series expansion for effective calculations.

3.4 Preprocessing

In the following I discuss the preprocessing of the field data and tomography models that is required to correctly forward simulate the waves and to be able to compare the synthetic data with the field data.

3.4.1 Data preprocessing

After reading in the raw data, converting it to SU format and checking the data quality by means of a visual inspection of the shot gathers as well as plotting the amplitude spectra (see section 3.2), further pre-processing steps are required to properly compare the field data with simulated waveforms later on.

Firstly, the sources and receivers have to be rotated into the borehole plane to define their exact position in the following simulations. This correction corresponds to a projection of the source and receiver coordinates onto the borehole plane. Secondly, I correct for the tilt of the receivers that is caused by the non-vertical boreholes. For this purpose, the traces are rotated such that the vertical components of the receivers are actually aligned with the vertical axis of the coordinate system. Thirdly, I have to transform the inherently 3D data to 2D, because the inversion software *IFOS2D* uses a 2D forward solver. It simulates point sources by means of a line source that extends indefinitely along the axis perpendicular to the x-z-plane, which is the borehole plane in this case. The transformation from 3D to 2D is required as the geometrical spreading of a point source differs from a line source both with respect to the amplitude and phase. A simulation of the wavefield would thus not be comparable to the field data.

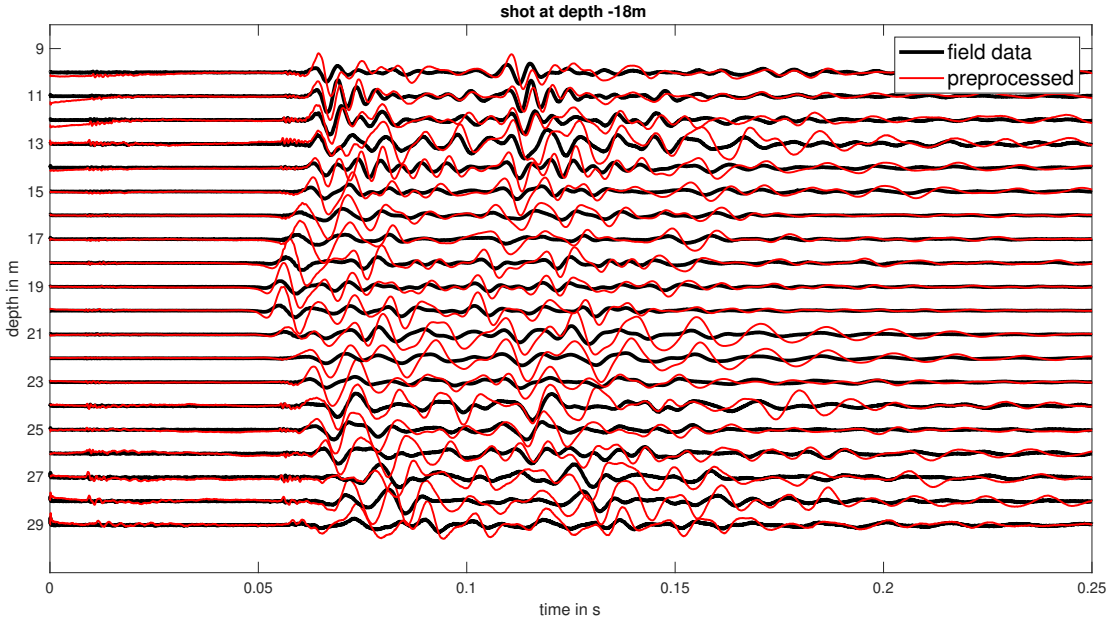

Figure 3.4: Pre-processed shot gather for a shot in 18 m depth. Shown is the raw field data in black and the pre-processed shot gather in red. Applying the 3D to 2D transformation increases the amplitudes of the waveforms.

In order to perform the conversion the so-called direct wave transformation proposed by Forbriger et al. (2014) is applied. It consists of a convolution with $\sqrt{t^{-1}}$, where t is time, and a multiplication with $\sqrt{t^{-1}}$, which acts as a time-domain taper. Subsequently, another multiplication with $r\sqrt{2}$ scales the waveforms dependent on the offset r. The preprocessed data is exemplarily shown for a shot depth of 18 m in Figure 3.4. It can be seen that the amplitudes are increased compared to the raw data due to the correction factors that are applied.

3.4.2 Model interpolation

As discussed in section 3.3, the models that were obtained by von Ketelhodt et al. (2019) by means of a separate isotropic and a joint anisotropic traveltime tomography are given in terms of v_{P}, v_{SV} and v_{SH} as well as v_{P0}, v_{S0}, ε, δ and γ, respectively. The latter three quantities are the so-called Thomsen parameters that were introduced in subsection 2.1.5 and the index zero indicates vertical velocities.

Procedure

First of all, the tomography models are interpolated using the approach by Bunks et al. (1995) to minimize the errors that are introduced in the least squares sense. This is achieved by interpolating the inverse of the velocities as it is proportional to the traveltime. The interpolation not only smooths the models, but also allows for a discretization of the models that fulfills the condition to avoid numerical grid dispersion, which is given by Equation 2.52 proposed in subsection 2.2.3. The minimum velocity in the tomography models is given by an S-wave velocity of about 158 m/s. The number of grid points per wavelength in case of a sixth-order FD scheme with Holberg coefficients is given by $n = 4.77$. The maximum frequency is chosen as twice the estimated source frequency. Based on the average amplitude spectrum in Figure 3.3 and considering that the Earth

acts as a low pass filter, the source frequency is assumed to be 150 Hz. Therefore, the maximum frequency is 300 Hz. The final grid spacing is chosen such that it is an even number in centimeters. This ensures that parameter updates during the inversion that might be smaller than the current minimum velocity still yield an accurate numerical simulation.

Secondly, boundary zones of 20 grid points are added at the left and right side as well as the bottom of the models.[4] This is required for an absorption of the simulated wavefield to avoid artificial reflections at the model boundaries. I assign the respective parameter values at the edges of the tomography models to the boundary points, i.e., I extend the models horizontally for the lateral boundaries and vertically for the bottom boundary with a constant value. In order to simulate the free surface it is necessary to apply the same procedure to the depth region from 0 to 10 m depth, because we lack information about this part of the subsurface.This would pose a significant source for errors in the simulation would we not only consider transmitted waves, but also reflections.

Apart from that, I require a density model. This can be derived from the P-wave velocity model via Gardner's equation (Gardner et al., 1974) that defines an empirical relation between the two parameters

$$\rho = 310\, v_{\mathrm{P}}^{0.25} \tag{3.3}$$

with the density ρ in kg/m^3 and the P-wave velocity v_{P}, the value of which has to be taken in m/s.

The resulting models with 400×220 grid points and a grid point spacing of $\Delta h = 0.08$ m are shown in Figures 3.5 and 3.6.

Model description

The isotropic P-wave velocities (see Figure 3.5, upper left) range from approximately 1540 m/s to 1890 m/s, the SV-wave velocity covers a range between 160 m/s and 480 m/s and the SH-wave velocity a narrower range between 200 m/s and 450 m/s. The density varies between approximately 1940 kg/m^3 and 2040 kg/m^3. Overall, the models are dominated by low-velocity or low-density structures, respectively, compared to their bounds.

Considering depths between 10 m and 30 m, the structure of the P-wave velocity model and the S-wave velocity models differs despite of the cross-gradient constraints that were applied. While the P-wave model indicates horizontal layering, the low-velocity structure of the S-wave models is interrupted by round high-velocity anomalies right of the center and in the deeper central part of the models. Whereas, those anomalies cannot be identified in the P-wave velocity model. However, there is a high-velocity layer in the upper part of up to 0.8 m thickness that can be found in the upper right corner of the SV-wave model as well, though to a smaller lateral extent. This is probably related to the coupling of P- and SV-waves. Below the high-velocity layer, one might recognize four to six more layers with alternating lower and higher velocities of varying thickness in the P-wave velocity model.

Further, the SV- and the SH-wave velocity models differ from each other, though to a smaller extent than the P-wave model. The high-velocity anomaly just below 10 m

[4] Note that additional boundary points are added to obtain an even number of grid points for easier computation on high performance computers.

depth is visible in the SH-model as well. However, it seems to be less thick and more extended towards the left boundary with an overall lower velocity.

The round high-velocity anomalies are located at the same positions at 20 m and 25 m depth with diameters of about 1.5 m and 2.5 m, respectively, although the lower one is more defined in the SH-model. Contrary to that, the one in the SV-model is more blurred into the high-velocity layer that can also be seen in the lower right corner of the P-model. Apart from that, the SH-model appears to have some layering structure like the P-model. The absence of this in the SV-model, though, might be attributed to the color scheme that is used to plot the models as it might be identified in the original models by von Ketelhodt et al. (2019). The structural similarity between the P-wave velocity and the density model is directly related to the way the density is determined.

The anisotropic velocity models that are presented in Figure 3.6 show the horizontal layering clearer than the isotropic models. However, the high-velocity anomaly right of the center of the S-wave model is less pronounced and the lower one almost vanishes compared to the background. The high-velocity layer at the top, though, now extends over the entire distance between the boreholes in the S-wave velocity model.

Additionally, the anisotropy parameters ε, δ and γ are shown in the lower row. While the ε model depicts some round anomalies that can be associated with locations of an increased S-wave velocity, the high δ anomaly that extends over almost the entire borehole distance at a depth of just below 20 m might yield to the slightly decreased P-wave velocity at that depth. However, the anomaly in the upper left corner does not seem to have that effect on the P-wave velocity model. The γ model shows some similarities with the S-wave model, although the round anomalies are very much smeared over the entire distance between the boreholes and might also be influenced by the P-wave model that has a similar, though reversed structure in that depth, i.e., low P-wave velocities approximately coincide with high γ values.

3.4.3 SV-wave anisotropy and quality of tomography results

The low values of ε and δ indicate very weak P-wave anisotropy. Von Ketelhodt et al. (2019) also show that the isotropic inversion yields smaller errors. Nevertheless, the SV-wave anisotropy is expected to be significant as it is controlled by the $v_\mathrm{P}/v_\mathrm{S}$-ratio which leads to a S-wave anisotropy between 2% and 20% for the values that are presented by von Ketelhodt et al. (2018, 2019). The cause of anisotropy is seen in the clay minerals and the anisotropic stress environment.

The resolution of the tomography was tested by means of checkerboard tests which showed that isolated higher ε values lie below the resolution limit of about 3×3 m. The maximum absolute error with respect to two standard deviations was determined from 100 different inversions to 80 m/s corresponding to 5% for the P-wave models and 40% for the S-wave models. Hence, the error is bigger than the anisotropy caused by the stress regime. Nevertheless, the assumption of an anisotropic media seems to be valid as the X-shaped distorsions in the S-wave velocity models that are attributed to anisotropy by von Ketelhodt et al. (2018) do not occur in the anisotropic tomography model.

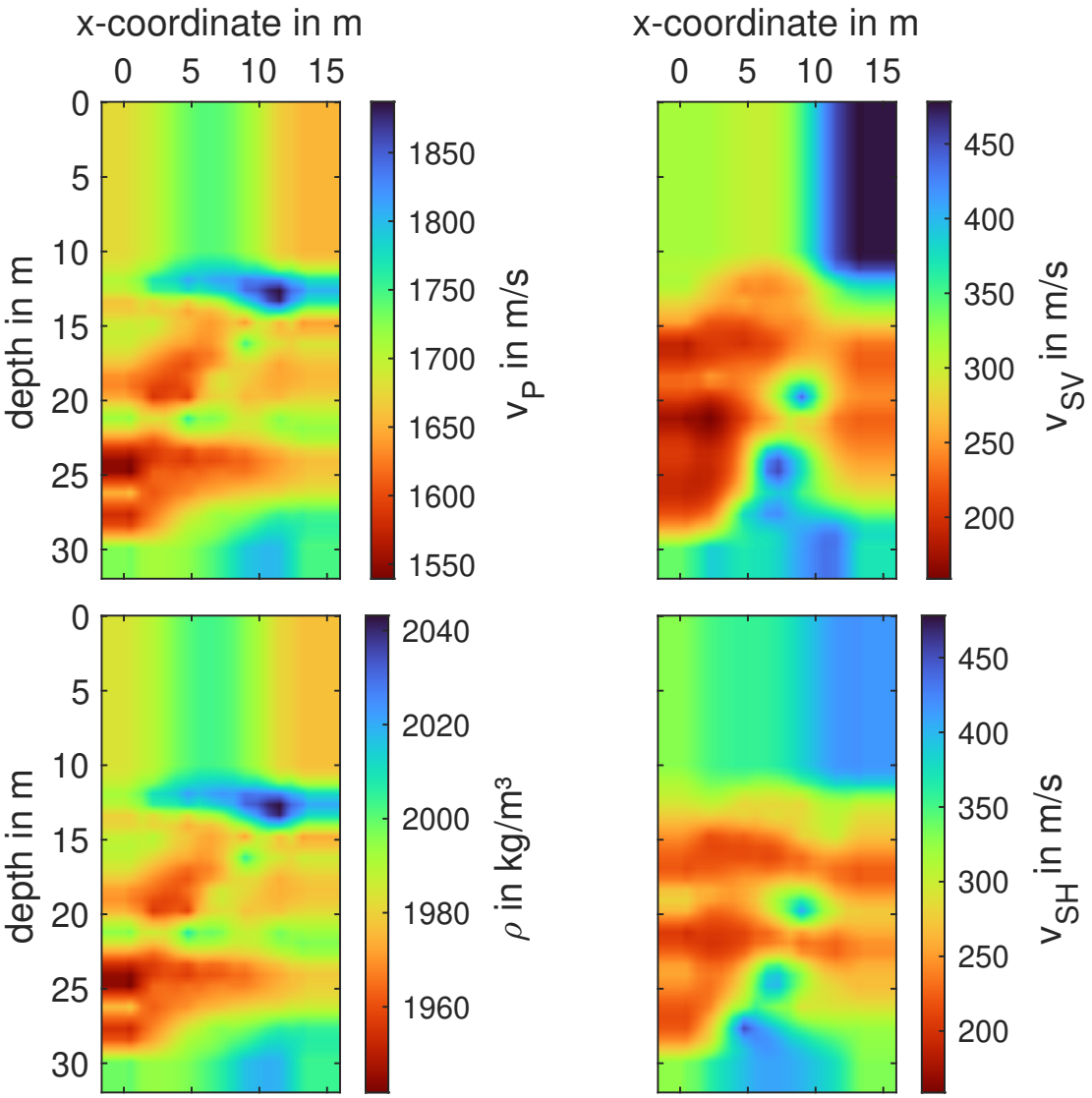

Figure 3.5: Shown are the velocity models (upper left: v_{P}, upper right: v_{SV} and lower right: v_{SH}) that were obtained by traveltime tomography in a separate isotropic inversion by von Ketelhodt et al. (2019) and the density model ρ (lower left) that is calculated based on the P-wave velocity and Gardner's equation.

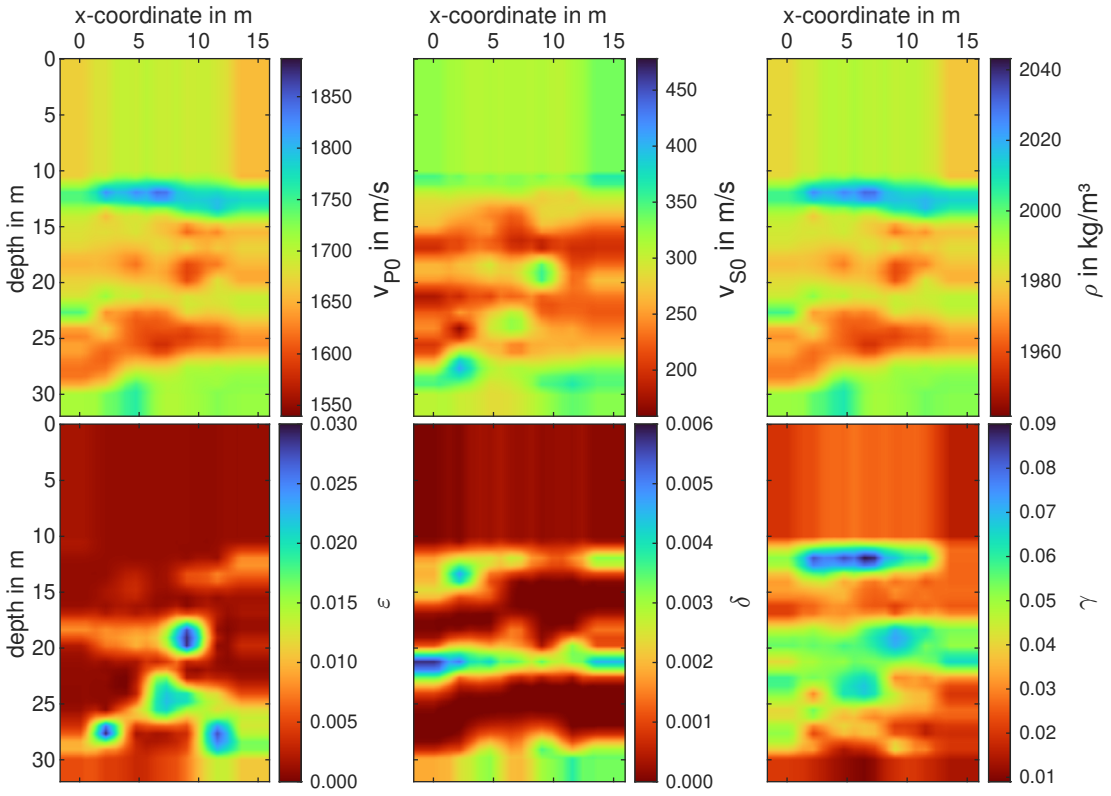

Figure 3.6: The figure shows the velocity models (upper left: v_{P}, upper center: v_{SV}) and the density model (upper right: ρ) as well as the Thomsen parameters (bottom row) that were obtained by traveltime tomography in a joint anisotropic inversion by von Ketelhodt et al. (2019). Again, ρ is calculated based on the P-wave velocity and Gardner's equation.

4. Forward modeling

As discussed in section 2.1, anisotropy manifests itself in a directional dependence of the stress-strain relation and, consequently, the wave propagation velocity. In case of the SV-wave this can yield an increase or decrease of the velocity with propagation directions up to 45°, while it is equal in vertical and horizontal direction. The wavefronts are, thus, no longer spherical in a homogeneous medium. In order to confirm the expectations from the theory of VTI wave propagation and to investigate the effect of anisotropy on the wavefield in the given crosswell setting, I forward-model it based on homogeneous models and the tomography models presented in subsection 3.4.2. For this purpose, two simulations using homogeneous models are performed that use the isotropic and anisotropic forward solver of the *IFOS2D* software, respectively. The results provide information on the anisotropy effect due to the theory of wave propagation in VTI media. Moreover, the additional effects due to the models' differences is initially estimated using homogeneous models with the mean isotropic and anisotropic velocities. Another comparison of the forward-modeled wavefield based on the tomography models reveals the differences between the synthetic waveforms and the field data. Eventually, viscoelastic simulations are performed to investigate the damping effect on the wavefield. The synthetic waveforms are once again examined regarding their onset times and the waveform fits.

4.1 Elastic forward modeling

4.1.1 Homogeneous models

In a first step to study VTI anisotropy, the homogeneous models are given by the mean velocities and density over all grid points of the anisotropic tomography models without the added boundary zones. The corresponding values can be found in Table 4.1. To simulate the isotropic wavefield I run the isotropic code and use the vertical anisotropic velocities. Figure 4.1 shows the synthetic shot gathers for a shot at 18 m depth, normalized to the maximum of the isotropic waveforms. As it is expected based on Equation 2.12, the SV-waves arrive earlier at receivers further up or down from the shot depth in the VTI case compared to the isotropic simulation. Thus, we can confirm that SV-waves propagate faster for phase angles $\theta \in]0°, 90°[$ for the mean values of the tomography. Furthermore, it can be seen that the amplitudes of the deeper traces are larger in the VTI case. These observations correspond to the results of the studies regarding the forward solver conducted by Krampe (2018). There, it was shown for a parameterization with ε and δ that the SV-waves have an almost quadratic wavefront with amplitudes towards the corners due to the velocity being highest at a phase angle of 45°. This, however, would not be the case if $\delta > \varepsilon$ or $\varepsilon < 0$ as such conditions would yield a minimum of the SV-wave velocity at 45°. While a strong free-surface reflection is observed in the isotropic simulation, it is missing in the anisotropic result. The snapshots in Figure 4.3

Table 4.1: Mean parameter values of anisotropic tomography models required in P/SV-case.

parameter	value
v_{P} in m/s	1680
v_{SV} in m/s	272
ρ in kg/m^3	1985
$v_{\mathrm{P,hor}}$ in m/s	1689
$v_{\mathrm{SV}}(45°)$ in m/s	316
ε	0.0052
δ	0.0011

Table 4.2: Mean parameter values of isotropic tomography models.

parameter	value
v_{P} in m/s	1692
v_{SV} in m/s	303
ρ in kg/m^3	1988

reveal strong amplitudes propagating non-horizontally in the isotropic case. In the VTI case, however, the amplitudes in that direction are significantly weaker and thus do not produce a visible free-surface reflection.

In a second step, the effect of the difference between the mean isotropic and anisotropic velocities along with the theory of isotropic and anisotropic wave propagation is estimated. For this purpose, homogeneous models using the mean isotropic velocities (see Table 4.2) are set up and input into the isotropic forward solver. Figure 4.2 shows the resulting, fully isotropic shot gather in contrast to the fully anisotropic waveforms. It becomes clear that the isotropic SV-wave velocity which is 31 m/s faster than the anisotropic mean (see Table 4.1 and Table 4.2), overcompensates the anisotropy effect regarding the velocity increase with increasing phase angle θ. Only the two traces from the deepest geophones show similar SV-wave onset times. This means that at a phase angle of around 40° the anisotropy of the SV-wave reaches the velocity of the isotropic model. In the source depth, however, the isotropic wavefield arrives approximately 7 ms earlier. Considering the exact distance between source and receiver of 13.49 m and to a greater extent their placement on the grid with the grid point spacing of $\Delta h = 0.08$ m, this result is in accordance with the expectation. Besides, the amplitudes in the horizontal directions with respect to the source position are slightly smaller in the VTI case than they are in the isotropic case. Towards shallower and deeper receivers, though, the amplitudes increase stronger than in the isotropic waveforms. Again, this matches the expectation on wave propagation in VTI media.

4.1.2 Tomography models

Running two forward simulations with the isotropic tomography models (see Figure 3.5) and the isotropic code as well as the anisotropic tomography models (see Figure 3.6) with the VTI code, the wavefields can be compared with respect to the effect of anisotropy in the medium. Figure 4.4 again depicts the Z-component of the shot gather with a shot at 18 m depth. Although one would expect earlier arrivals at the shallow and

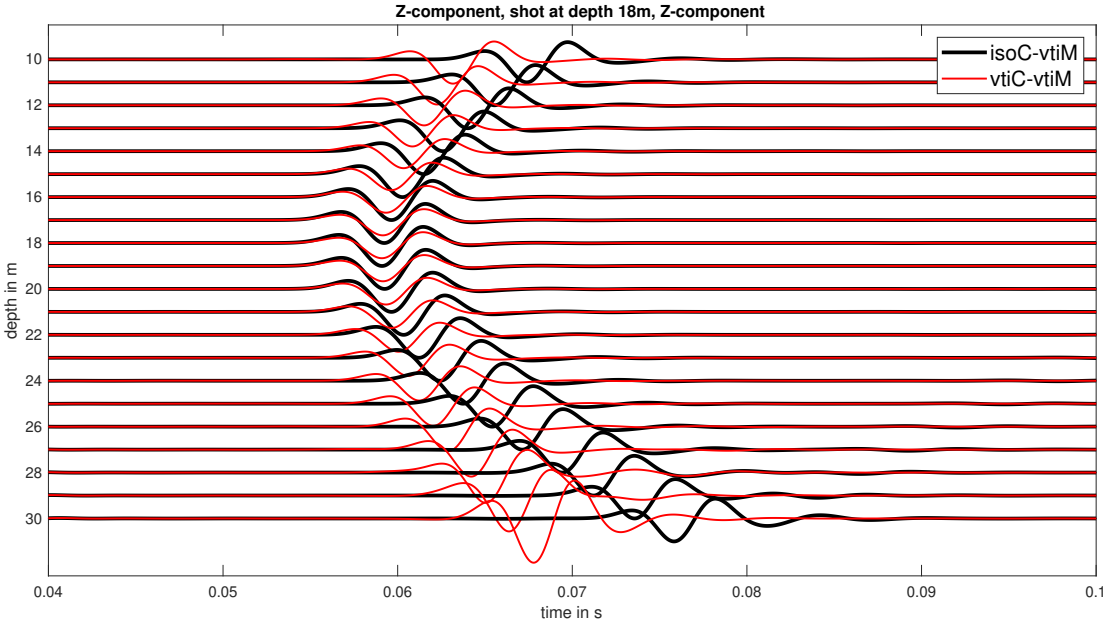

Figure 4.1: Effect of VTI theory on the wavefield using homogeneous models. The shot is triggered in a depth of 18 m and the waves arrive earliest at the receiver at the same depth. At receivers further up and down the waves arrive increasingly earlier in the VTI case compared to the isotropic case.

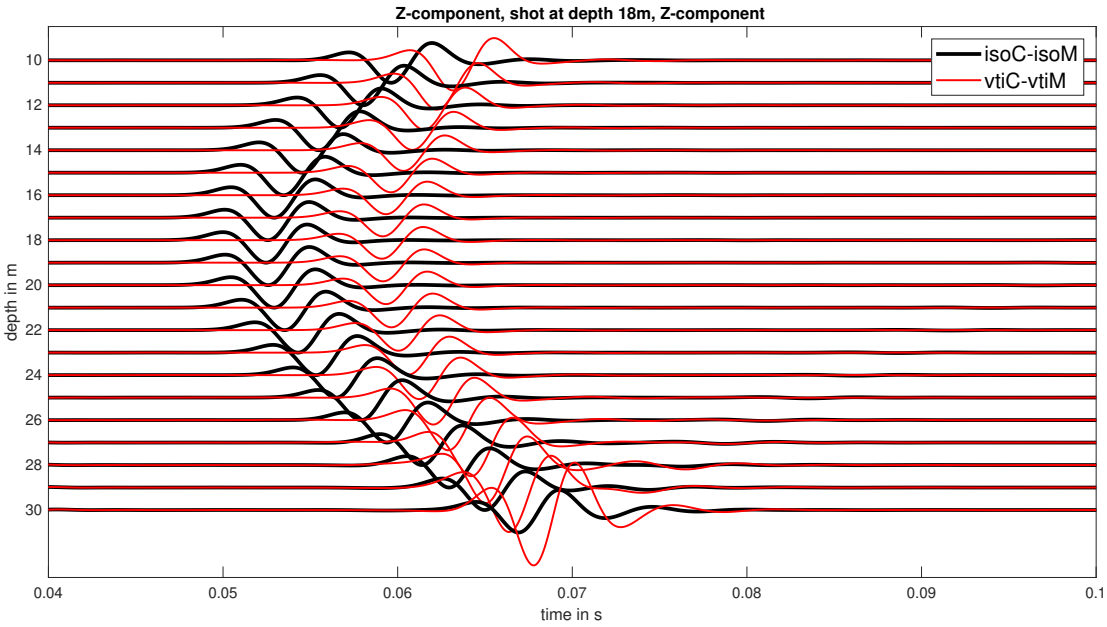

Figure 4.2: Effect of VTI theory and mean velocity difference on the wavefield using homogeneous models. The shot is triggered in a depth of 18 m and the waves arrive earliest at the receiver at the same depth. At receivers further up and down the waves have increasingly larger amplitudes in the VTI case compared to the isotropic case. Due to the higher mean velocity of the isotropic models, though, the anisotropy effect is overcompensated.

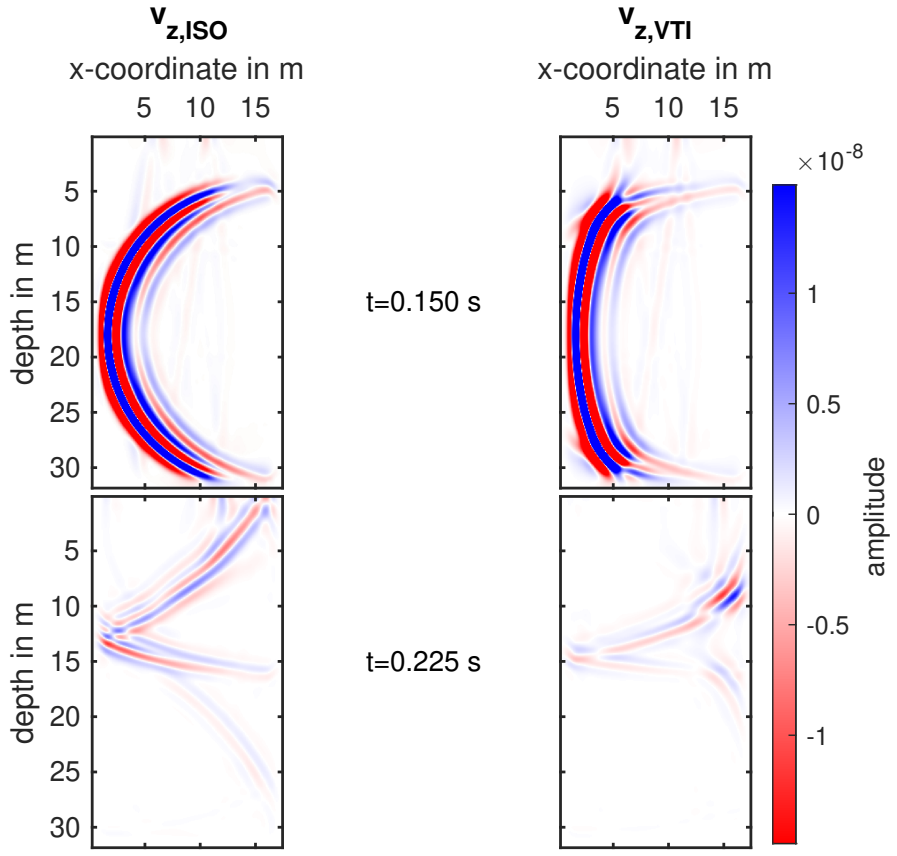

Figure 4.3: Snapshots of the forward-modeled wavefield using the isotropic and VTI code, respectively. In the upper row two snapshots at $t = 0.15\,\mathrm{s}$ are presented. The wavefield modeled with the isotropic code on the left hand side reveals a circular wavefront in the y-component of the particle velocity field. This yields large amplitudes in non-horizontal directions. Contrary to that, the wavefront arising from the VTI simulation is much less curved with maximum amplitudes at about 45° from the source position. Closer towards the vertical, the amplitudes become extremely weak. At a later time step of $t = 0.225\,\mathrm{s}$ the surface reflections can be observed. The isotropic simulation produces a comparably high-amplitude free-surface reflection, while it is significantly weaker in the VTI case. Here, again, large amplitudes can be identified in a direction of about 45° towards the lower right side of the model space.

deep receivers in the anisotropic simulation, this cannot be observed. Instead, the SV-waves arrive even later in the VTI simulation, as for instance at the receiver in 30 m depth. This can, however, be explained by the higher mean velocities and especially their distribution in the isotropic models that apparently compensate for the anisotropy effect. In comparison with Figure 4.2 it also has to be taken into account that the velocities in the part of the anisotropic model through which the wave has traveled are, to a large extent, lower than the mean velocity (see Figure 3.6). As a result the anisotropy effect cannot compensate for the higher velocities in the isotropic model.

In anticipation of FWI it is interesting to note that the onset times of the two simulations vary less than half a wavelength, i.e., there is no cycle skipping, which is the criterion for the inversion to converge to the correct model. This implies that both tomography models should be good enough to allow reaching the correct minimum of the misfit function. Contrary to the matching onset times, the waveforms differ considerably, especially in shallow depths where the anisotropic simulation produces large amplitudes at late arrival times. However, this is precisely the strength of FWI that fits not only the onsets but the complete waveforms.

A comparison with the field data in Figure 4.5 (left) reveals a time shift at the onset of the SV-wave by about 5.5 ms in the trace recorded at the depth of the source. This is caused by the assumption of a Ricker wavelet as an initial source wavelet. Even though a time delay is applied to the Ricker wavelet to make it causal, it is not a physical wavelet as it is zero-phase. Physical source signals, though, are ideally minimum-phase, i.e., their energy buildup is concentrated at the onset. A suitable source signal can be obtained by performing a source time function inversion of the field data. In order to make it easier to compare the waveforms, I correct the time shift by shifting the entire shot gather by 5.5 ms even though the time shift varies from trace to trace. Then the SV-waves that propagated horizontally and hence are unaffected by anisotropy match in terms of the onset times. The resulting shot gather is presented in Figure 4.5 (right). It can be seen that the forward-modeled wavefield arrives earlier than the observed data in depths from 25 to 29 m. Apart from that, there appears a polarity reversal between 23 and 29 m depth when comparing the onsets.

Furthermore, the forward-modeled wavefield is much less complex than the observed one. Again, the source signature will highly influence the shape of the waveforms and thus has to be considered as a substantial factor when comparing the observed waveforms. Apart from that, 3D effects that occur in the field cannot be modeled by the 2D software and based on the 2D models. Neighboring boreholes are significant sources for diffraction and will therefore also alter the wavefield. Additionally, it is neglected that the boreholes themselves are cavities and hence create an impedance contrast to the surrounding medium. Due to that the borehole walls can act as secondary sources, which will further increase the complexity of the wavefield. It should be noted, though, that the diameter of the boreholes of around 0.3 m is only about four times the grid spacing of 0.08 m and hence can not properly be modeled with the given configuration in the simulation anyway. This would, for example, require a variable grid discretization as Wu and Harris (2003) suggest. Eventually, the water table depth and gravel layers form a poro-elastic medium, which is not considered in the simulation.

4.2 Viscoelastic anisotropic forward modeling

Real media are not perfectly elastic, hence assuming a viscoelastic medium should improve the simulation of the wavefield. The anelastic behavior of the medium attenuates

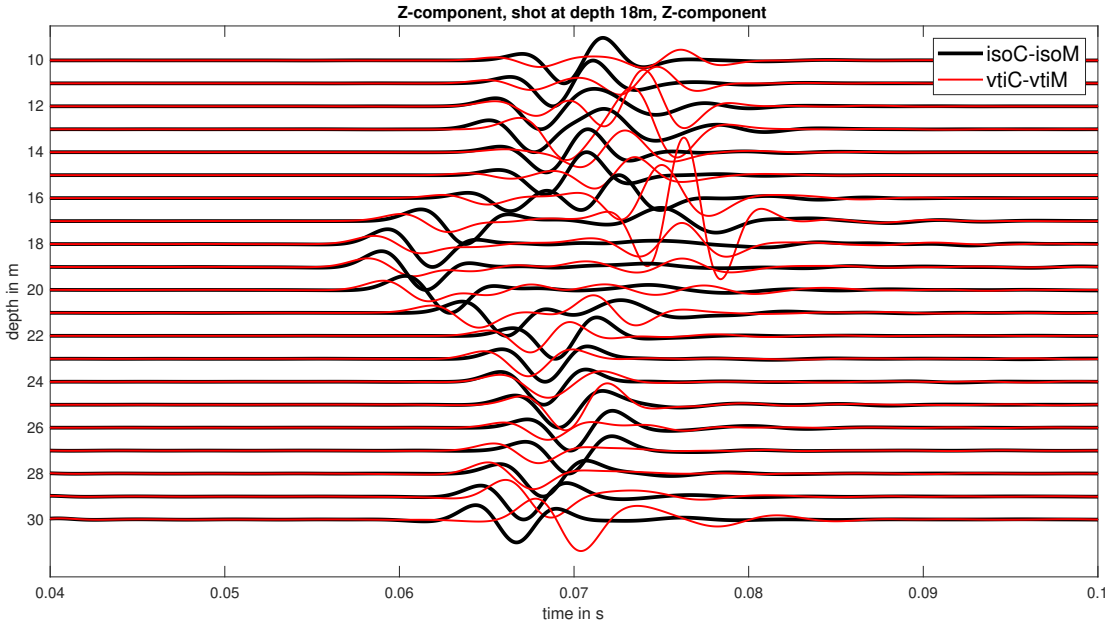

Figure 4.4: Comparison of isotropic and anisotropic waveforms. The shot gather shows the Z-component. No systematic difference in arrival times of the SV-wave that could be attributed to anisotropy can be observed.

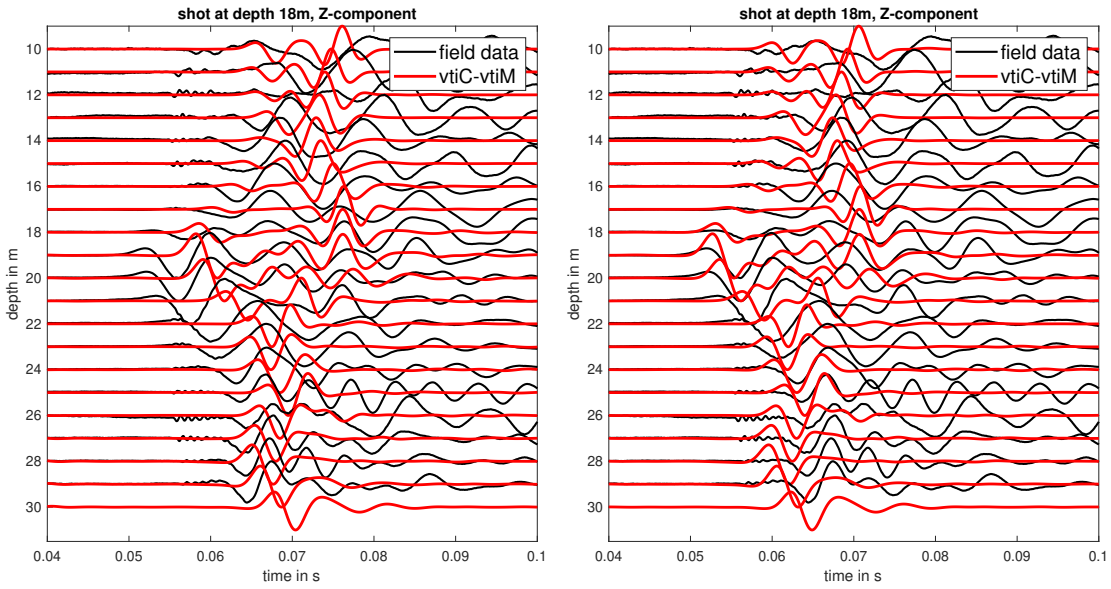

Figure 4.5: Comparison of elastic VTI simulation and field data. The shot gathers show the Z-component. To match the onset time of the SV-wave in the source depth the forward-simulated wavefield is shifted by 5.5 ms in the shot gather on the right-hand side. Nevertheless, the forward-modeled onset times differ from those of the field observation by a varying extent.

the amplitudes of the waves that propagate through it and introduces dispersion. To simulate these phenomena a model for the quality factor Q is required, which allows to determine relaxation times as described in subsection 2.1.7. The quality factor is estimated by the spectral ratio method and approximated by the extended τ-method. Finally, the viscoelastic anisotropic wavefield based on the anisotropic tomography models is compared to the elastic one.

4.2.1 Quality factor estimation

A Q value that fits the subsurface conditions of the field data can be derived by the spectral ratio method (Tonn, 1989), that was initially derived for vertical seismic profiling (VSP) data referring to a transmission geometry. The method uses the fact that the amplitudes decay with offset depending on frequency. In order to apply the method, recordings at two different offsets $x_i\,(i = 1, 2)$ with $x_2 > x_1$ are required. Then the amplitude spectra $|P_1|$ and $|P_2|$ need to be calculated. Their logarithmic ratio is given by

$$\ln\left(\frac{|P_2|}{|P_1|}\right) = -\omega\,\frac{x_2 - x_1}{2\,c(\omega_0)\,Q} \tag{4.1}$$

where ω is the angular frequency in rad/s, $c(\omega_0)$ the phase velocity in m/s at a reference frequency ω_0. Plotting the left-hand side of the equation over the angular frequency ω, the quality factor Q can then be determined from the linear slope m by

$$Q = -\frac{x_2 - x_1}{2\,c(\omega_0)\,m}\,. \tag{4.2}$$

Here, the spectral ratio method as implemented in the CREWES Q-estimator tool is applied. To analyze the field data, I again focus on the S-waves and sort the shot gathers by offset. This allows to define a time sampling interval, a dominant source frequency, a time window length, such that the window contains the transmitted SV-waves when calculating the spectra, as well as the starting times for the spectral estimate. Based on those parameters the tool generates synthetic traces of minimum-phase wavelets for an impulse source. Afterwards the amplitude spectra and the spectral ratio are determined. Lastly, the latter is fitted by a linear least-squares fit in the defined frequency range. The spectral ratio and the corresponding fit are exemplarily shown for a shot in 18 m depth in Figure 4.6. The fit is clearly dominated by the decreasing logarithmic spectral ratio below 50 Hz. Thus, the determined Q value, which is inversely proportional to the slope of the fit, might be too large. This implies that high frequencies are damped too weakly and low frequencies too strongly. However, with just one constant Q value for the broad frequency range of the field data, there is a certain trade-off and a compromise has to be found. Running the tool for all shots yields an average Q value of 20. Thus, the waves are moderately attenuated under near-surface conditions and weakly dispersive.

4.2.2 Q approximation

A constant Q value can be approximated by the τ-method proposed by Blanch et al. (1995). It allows to model L relaxation mechanisms by the relaxation frequencies f_l and the variable τ only, assuming weak absorption. In case of a constant Q less than 20 the Q value approximated by the relaxation frequencies is larger than the desired one. An optimization of the relaxation frequencies can be achieved by the extended τ-method introduced by Bohlen (1998) that considers a certain frequency range and minimizes the residuals applying the Levenberg-Marquardt method after weighting the

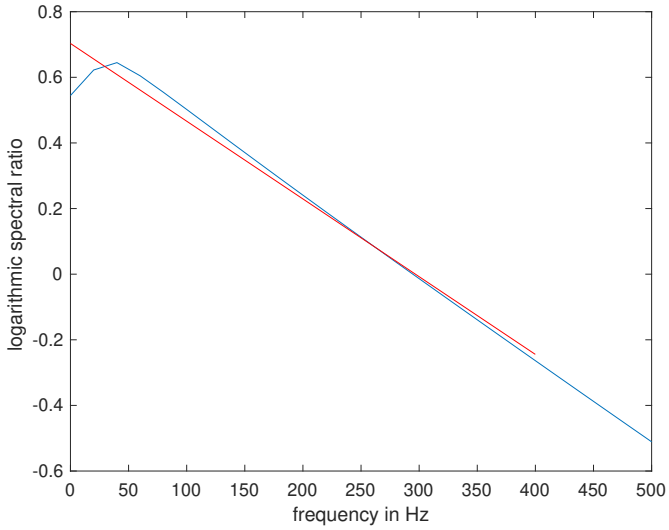

Figure 4.6: Logarithmic spectral ratio over frequency. The logarithmic spectral ratio (blue curve) is fitted up to 400 Hz (red line), which corresponds to the frequency up to which a contribution to the signal is observed for the field data.

Table 4.3: Relaxation frequencies $f_l = 1/(2\pi\tau_{\sigma l})$ and τ. The values are obtained using the extended τ-method introduced by Bohlen (1998) that weights and minimizes the squared residuals with respect to the frequencies of interest.

parameter	value
τ in s	0.0990
f_1 in Hz	1.88
f_2 in Hz	29.51
f_3 in Hz	295.84

residuals depending on frequency. Thus, it provides a good approximation of Q even at low frequencies and strong damping.

The previously estimated Q value of 20 is approximated by three relaxation mechanisms. The corresponding relaxation frequencies f_l and τ are given in Table 4.3. Three relaxation mechanisms is the minimum required to accurately model attenuation by a constant Q value. However, a large number of relaxation mechanisms increases the computational cost significantly such that a compromise has to be found. Figure 4.7 shows the approximated Q value Q_{approx} in reference to the desired one Q_0. It can be seen that it varies roughly by less than ± 3 with the largest deviations below 75 Hz and a maximum deviation at f_2 of about 2.5 when neglecting the value at zero frequency. Even though that variation is about six times larger than the difference of the values that are found in the Q estimation from the field data of the individual shot gathers of 19.68 to 20.48 from the average, the approximation is considered appropriate with respect to the computational cost.

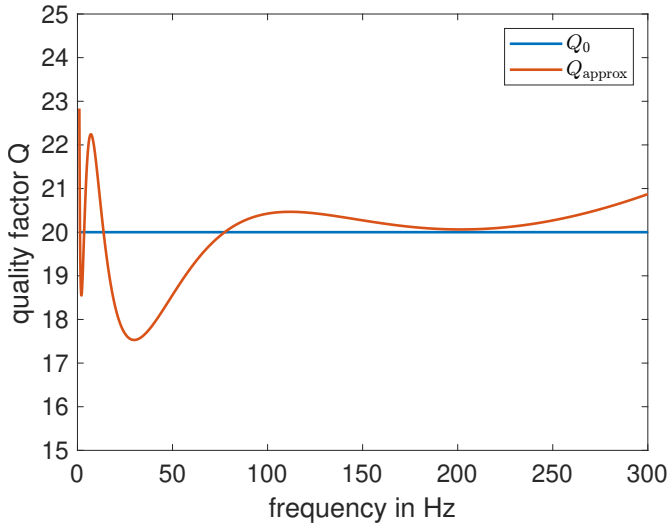

Figure 4.7: Approximated Q based on the extended τ-method introduced by Bohlen (1998) where three relaxation mechanisms are chosen. The determined relaxation frequencies and τ can be found in Table 4.3. The approximated Q values deviate from the desired value of 20 by about 2.5 at $f_2 = 29.51\,\text{Hz}$.

4.2.3 Viscoelastic forward modeling

As the viscoelastic simulations based on the homogeneous models become unstable even though the numerical stability criteria (see Equation 2.53 and Equation 2.54) are fulfilled and the cause of the instabilities remains unknown, the anisotropic tomography model is used to investigate the effect of damping on the wavefield.

Tomography models

The effect of attenuation on the wavefield is investigated by a comparison of the elastic and viscoelastic anisotropic simulation using the anisotropic tomography models (see Figure 4.8). The damping effect is clearly visible with reduced S-wave amplitudes compared to the elastic simulation. Due to that, the later arrivals in intermediate depth become very smooth, i.e., deeper frequent, in the viscoelastic results, while the elastic wavefield has some more wiggles there.

By normalizing each trace to its maximum the difference of the waveforms apart from the amplitude decay can be analyzed more thoroughly (see Figure 4.9). It can be seen that the viscoelastic wavefield arrives up to 1.5 ms earlier compared to the elastic one. Moreover, the early arrivals tend to have slightly larger amplitudes in the viscoelastic simulation, whereas later arrivals have smaller amplitudes in depths around 22 m.

Due to the time shift between the onsets from the elastic and the viscoelastic simulation, the time shift that is applied to properly compare the field data, is given by 4 ms in the viscoelastic case. Both the shot gather without shifting and the one with shifting are depicted in Figure 4.10. The amplitudes are normalized to the maximum amplitude of the observed and the simulated shot gather, respectively, as the former's amplitudes are much higher. This suggests that the attenuation of the subsurface is weaker than it is estimated by the Q-factor estimation via the CREWES tool.

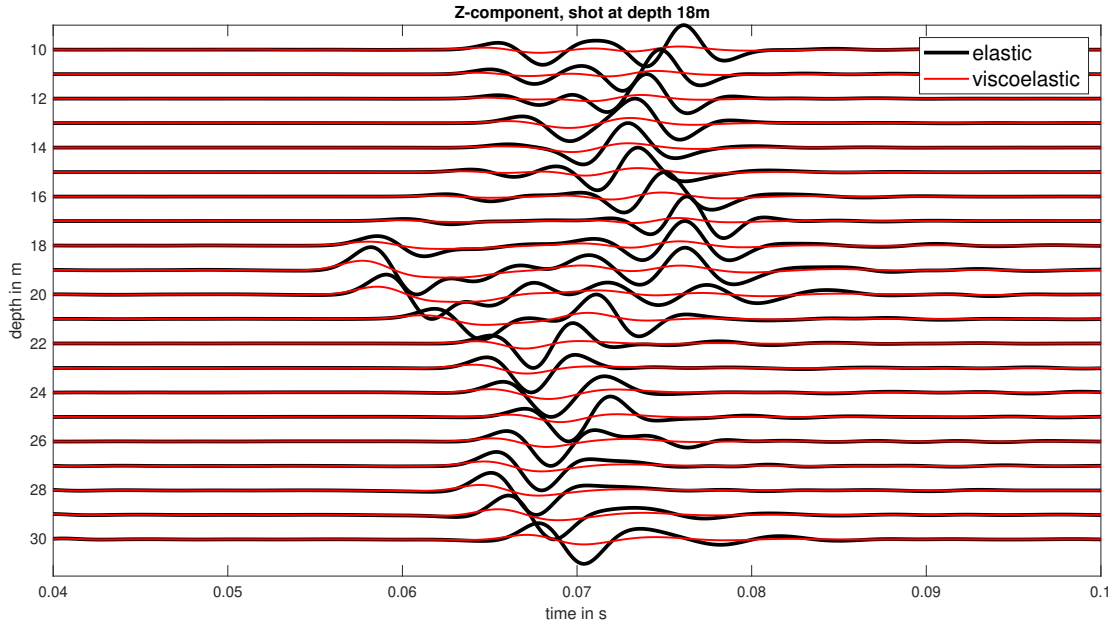

Figure 4.8: Comparison of elastic and viscoelastic VTI simulation with anisotropic tomography models normalized to overall amplitude maximum.

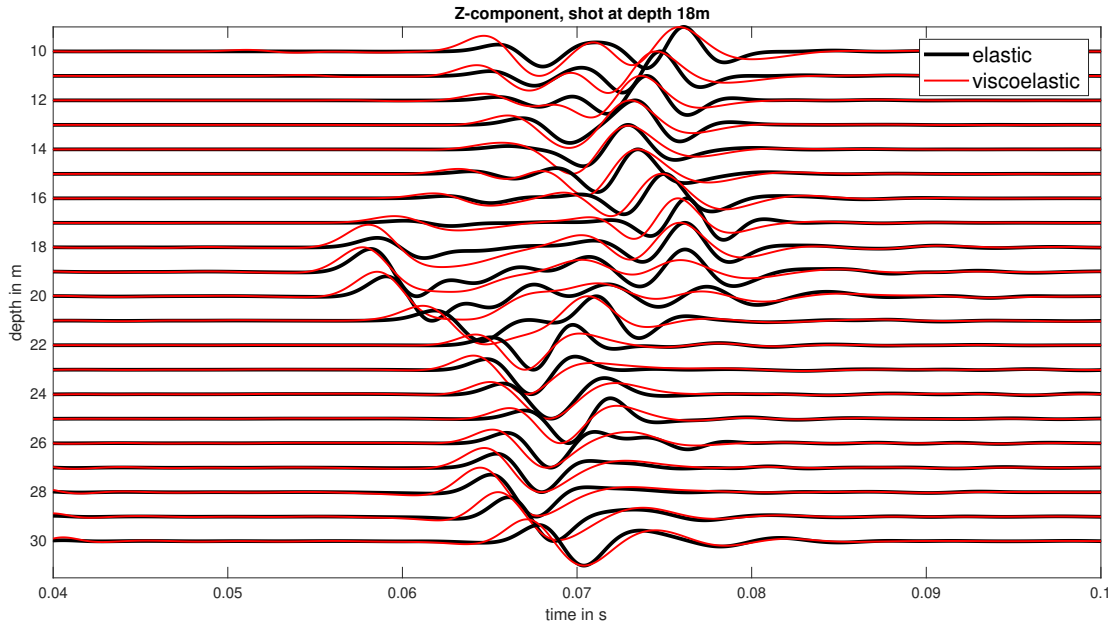

Figure 4.9: Comparison of elastic and viscoelastic VTI simulation with anisotropic tomography models normalized to trace maximum.

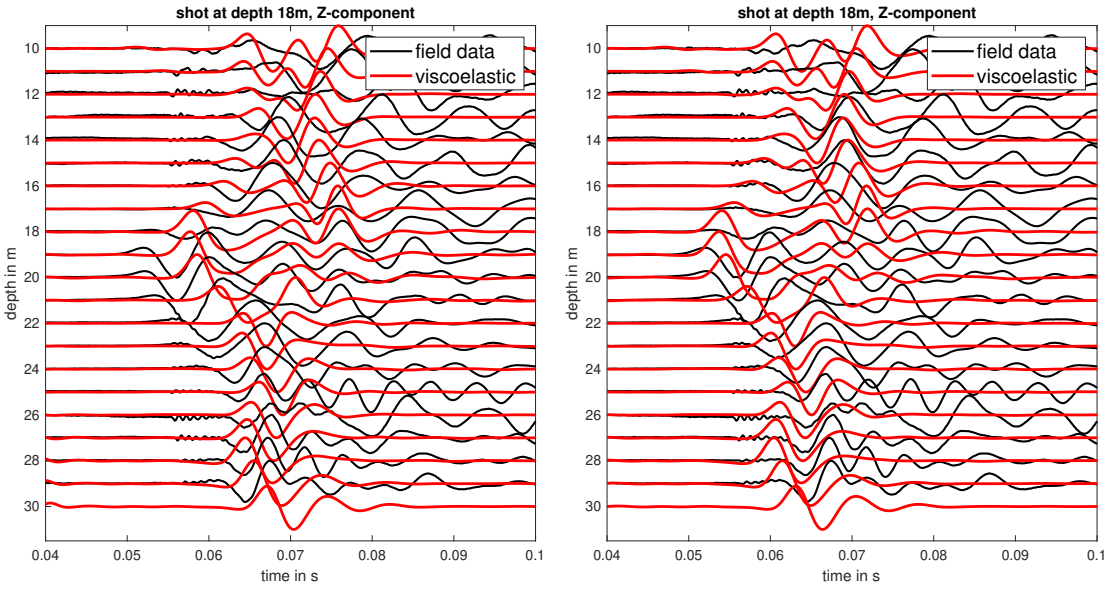

Figure 4.10: Comparison of viscoelastic VTI simulation and field data. The shot gathers show the Z-component. To match the onset time of the SV-wave in the source depth the forward simulated wavefield is shifted by 4 ms in the shot gather on the right hand side. Nevertheless, the forward modeled onset times differ from those of the field observation by a varying extent.

4.3 Concluding remarks

The forward simulations of the wavefield based on different models and assumptions of the subsurface properties, i.e., isotropy or anisotropy and elasticity or viscoelasticity, can produced substantial differences in the forward-modeled waveforms.

An issue that might arise from an unfitting hypothesis about the isotropy of the subsurface or the lack thereof is cycle skipping. This means that the onset times of the waveforms differ by more than half a period and prohibits convergence to the global minimum of the misfit function later on in the inversion.

On another note it is shown that the consideration of attenuation significantly dampens the amplitudes and introduces weak dispersion. In the case of very weak anisotropy that would not cause cycle skipping for the given geometry, the dispersion might ultimately introduce cycle skipping once again.

Comparisons of the elastically and viscoelastically forward-modeled waveforms with the field data have finally shown that there is a certain time-shift that also varies from trace to trace. This demonstrates that a source time function inversion will be required to obtain a more suitable source wavelet than the time-shifted Ricker wavelet that is used here if the field data is inverted.

5. Synthetic inversion tests

In the following, the isotropic and VTI gradient parameterizations are tested and compared with respect to their performance in the given crosswell setting for the elastic case. For this purpose, the reconstruction of low-velocity anomalies in the S-wave velocity models is investigated. According to Fermat's principle the wave will propagate through the medium such that its traveltime is minimized. Thus, it will avoid the low-velocity anomaly, which is consequently more challenging to reconstruct. Their velocity is reduced by 4% compared to the background model to ensure stable inversions for both the isotropic and VTI case. In order to focus on the S-wave anisotropy, that is parameterized in terms of the vertical SV-wave velocity v_{SV} and the SV-wave velocity in a direction of 45°, and to reduce the degrees of freedom, I invert for the S-wave velocity models only while keeping the P-wave velocity and density models constant at their true values.

At first, the anomaly is put in the center of the homogeneous S-wave models that are defined in Table 4.2 and Table 4.1, such that the anomaly is equally illuminated by waves originating above and below. Here, center refers to intermediate depth with respect to source depths of 10 to 30 m. Afterwards, the anomaly is shifted further to shallower source and receiver depths to assess the aperture. Finally, the anomaly is placed at different locations in the two anisotropic SV-wave velocity models, i.e., one above the other, to study the crosstalk between the VTI SV-wave velocity parameters v_{SV} and $v_{\mathrm{SV}}(45°)$. In all cases, forward simulations are run to generate synthetic data and the homogeneous models without anomalies are used as starting models in the inversion.

5.1 Reconstruction tests with square anomaly

In order to investigate how well an anomaly can be reconstructed when large parts of the wavefield pass through a feature in the subsurface horizontally and equally many waves originate above and below it, I introduce a square low-velocity anomaly of 3×3 m in the center of the v_{SV} and $v_{\mathrm{SV}}(45°)$ model with the top edge in 18.48 m depth. The extensions of the anomaly correspond to the resolution limit of the tomography (see subsection 3.4.3) and hence also allow to compare the two methods. Due to the square shape of the anomalies the results will provide direct information about the vertical and horizontal resolution that can be achieved in the inversion. This test is in the following referred to as "the" reconstruction test.

5.1.1 Isotropic code and isotropic models

Firstly, the fully isotropic case is studied using the isotropic code and isotropic models. The true S-wave model with a square anomaly in the center of precisely 290.88 m/s is shown in Figure 5.1(a). In order to prevent instabilities at the source and receiver locations, circular tapers with a radius of 1 m using a log-function are applied at these

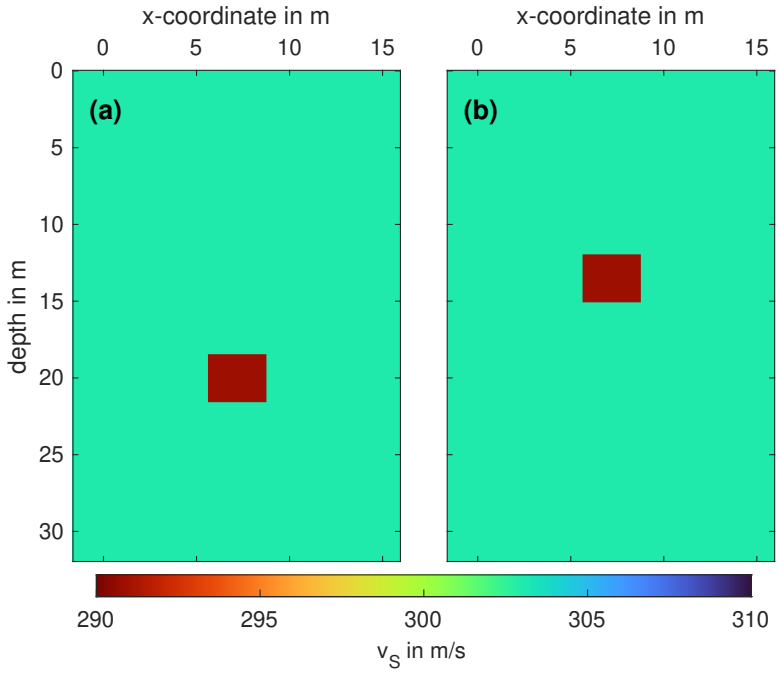

Figure 5.1: True isotropic SV-wave velocity models. The background model is given by the isotropic tomography model with $v_{\mathrm{SV}} = 303\,\mathrm{m/s}$. The velocity of the anomaly is 290.88 m/s. Model (a) is used to perform a reconstruction test with maximum illumination of the anomaly. The aperture is studied using model (b), where more waves originate at locations below the anomaly than above.

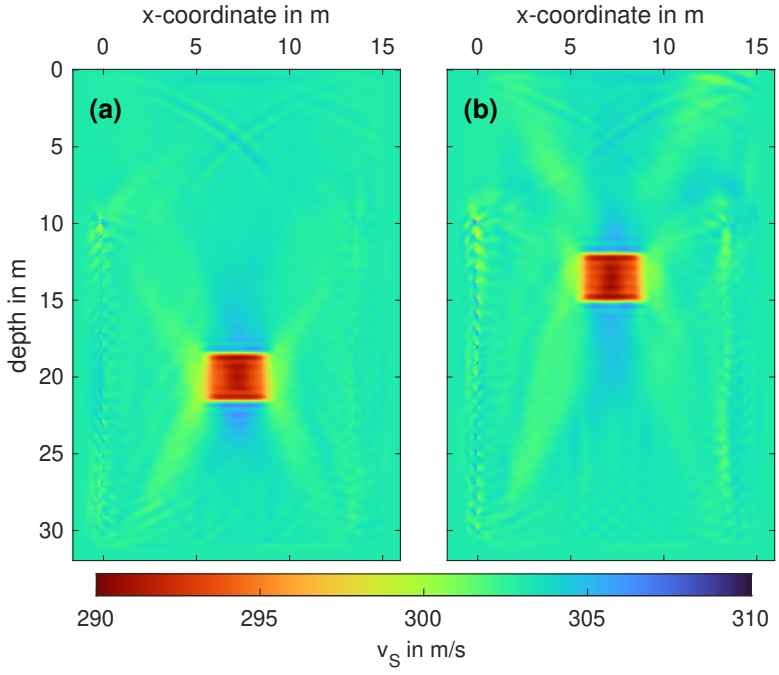

Figure 5.2: Inverted isotropic SV-wave velocity models. Model (a) shows the reconstruction of a square anomaly of $3 \times 3\,\mathrm{m}$ with maximum illumination. The aperture test result is presented in (b). In both cases X-shaped artifacts can be observed. The reconstruction of the anomaly in (a) and (b) is of similar quality.

positions. The extreme velocity values occur there because of high gradients that yield large parameter updates.

The result of the inversion is presented in Figure 5.2(a). It can be seen that the anomaly can be reconstructed at the correct location and in the true shape. Besides, the 4% lower velocity compared to the background model is almost reached at many grid points. This is especially the case at the top and bottom of the anomaly as well as for a vertical strip of about 0.8 m width in the center. The minimum difference to the true anomaly value is less than -1 m/s. At the edges of the anomaly the reconstructed velocities lie between the true background model's and the anomaly's velocity at about 298 m/s. Another feature of the inverted model can be found directly above and to a greater extent below the anomaly, where horizontal stripes with velocities higher than the background model appear with a regular distance of about 0.64 m. Their lateral extent is almost as large as the anomaly close to it and decreases with increasing distance forming an almost triangular shape. On top of that, X-shaped artifacts, that begin at the corners of the anomaly and extent towards the uppermost and lowermost receiver (left side) and source (right side) locations, are evident. Their velocities are slightly decreased compared to the background model. These artifacts are typical for this kind of reconstruction test and have also been observed by Hadden et al. (2019). Another X-shaped artifact with velocities that are in this case slightly higher than those of the background model can be seen in 0 to 8 m depth.

The inversion runs for 125 iterations until the step length estimation fails because it cannot find a step length that would further minimize the misfit. The corresponding evolution of the normalized L2 misfit is shown in Figure 5.3 (left) in black. During the first 16 iterations the misfit decreases strongly down to about $1.3 \cdot 10^{-3}$. Afterwards, the curve flattens until the normalized L2 misfit reaches its final value that lies in the order of 10^{-5}.

A comparison of the forward-modeled and the recovered seismograms reveals that the waveforms do not differ by eye (see Figure 5.6 (left)). The waveforms based on the initial model, though, are already quite close to the forward-modeled synthetics and deviate solely at depths below 17 m. While the onset times seem to coincide the phase and to a lesser extent the amplitudes are slightly different.

5.1.2 Anisotropic code and anisotropic models

After the isotropic case, the VTI case is studied using the VTI code and models. The true SV-wave velocity models are shown in Figure 5.4.[5] The low-velocity anomaly is located at the same position in both models. Again, the anomaly's velocity is reduced by 4% compared to the background. The velocities of the anomalies are, hence, given by 261.12 m/s for the vertical SV-wave velocity and 303.36 m/s for $v_{\mathrm{SV}}(45°)$, respectively. Thus, both the background and the anomaly velocities are higher in the $v_{\mathrm{SV}}(45°)$ models. Just like in the fully isotropic inversion, circular source and receiver tapers using a log-function are applied to prevent instabilities at these locations.

[5] Note that the colorbars range from 250 m/s to 290 m/s for v_{SV} and from 290 m/s to 330 m/s for $v_{\mathrm{SV}}(45°)$, respectively.

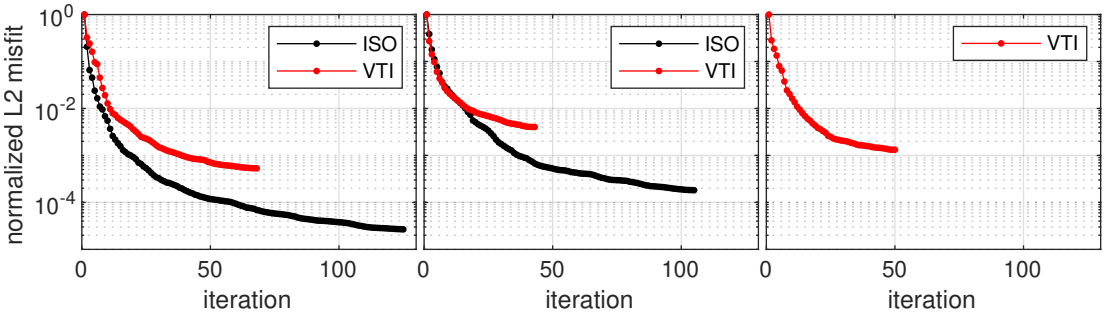

Figure 5.3: Normalized misfit evolution. Inversions performed with the isotropic code are shown in black, those with the VTI code in red. Left: Anomaly in center, center: aperture test with anomaly in 12 to 15 m depth, right: VTI crosstalk test. All in all, the isotropic inversions produce a smaller final normalized L2 misfit compared to the VTI inversion that also converges at a smaller number of iterations.

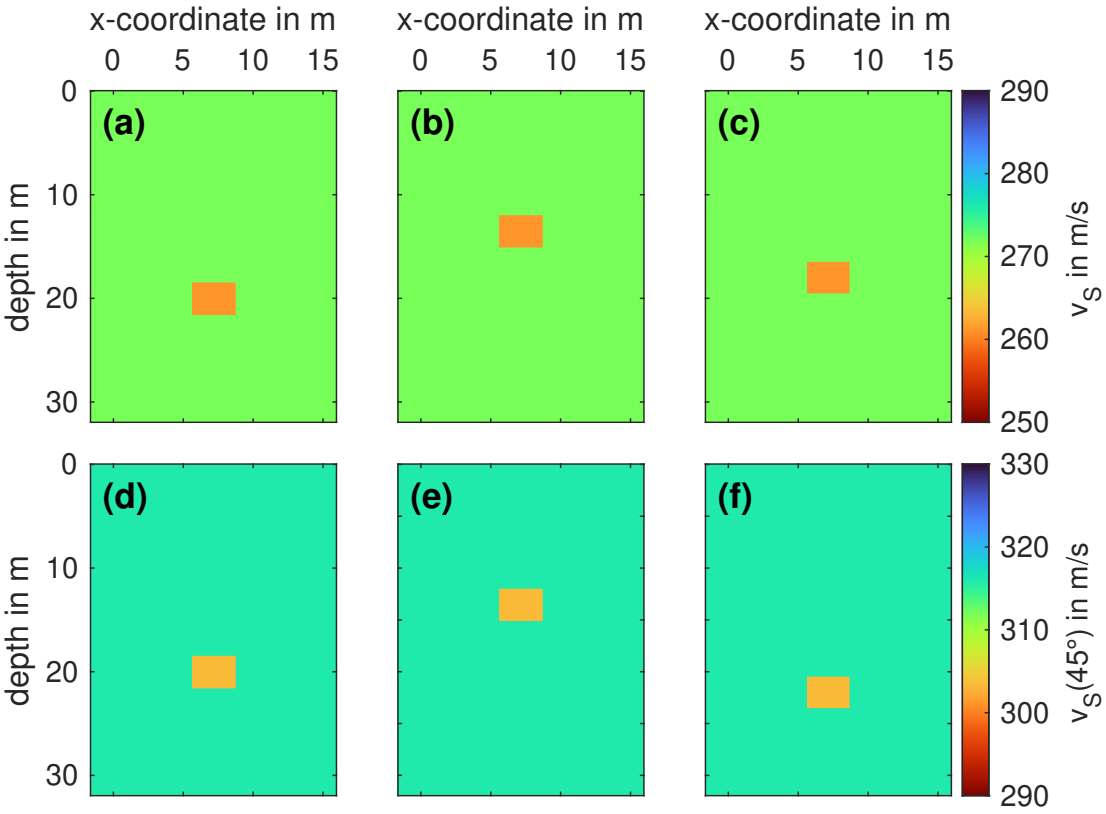

Figure 5.4: True anisotropic SV-wave velocity models. The background model is given by the respective anisotropic tomography model. The velocities of the anomalies are $v_{\mathrm{SV,a}} = 261.12\,\mathrm{m/s}$ and $v_{\mathrm{SV,a}}(45°) = 303.36\,\mathrm{m/s}$, respectively. The models (a) and (d) are used to perform a reconstruction test with maximum illumination of the anomaly. The aperture is studied using the models (b) and (e). Crosstalk between the SV-wave velocity models is investigated with the models (c) and (f).

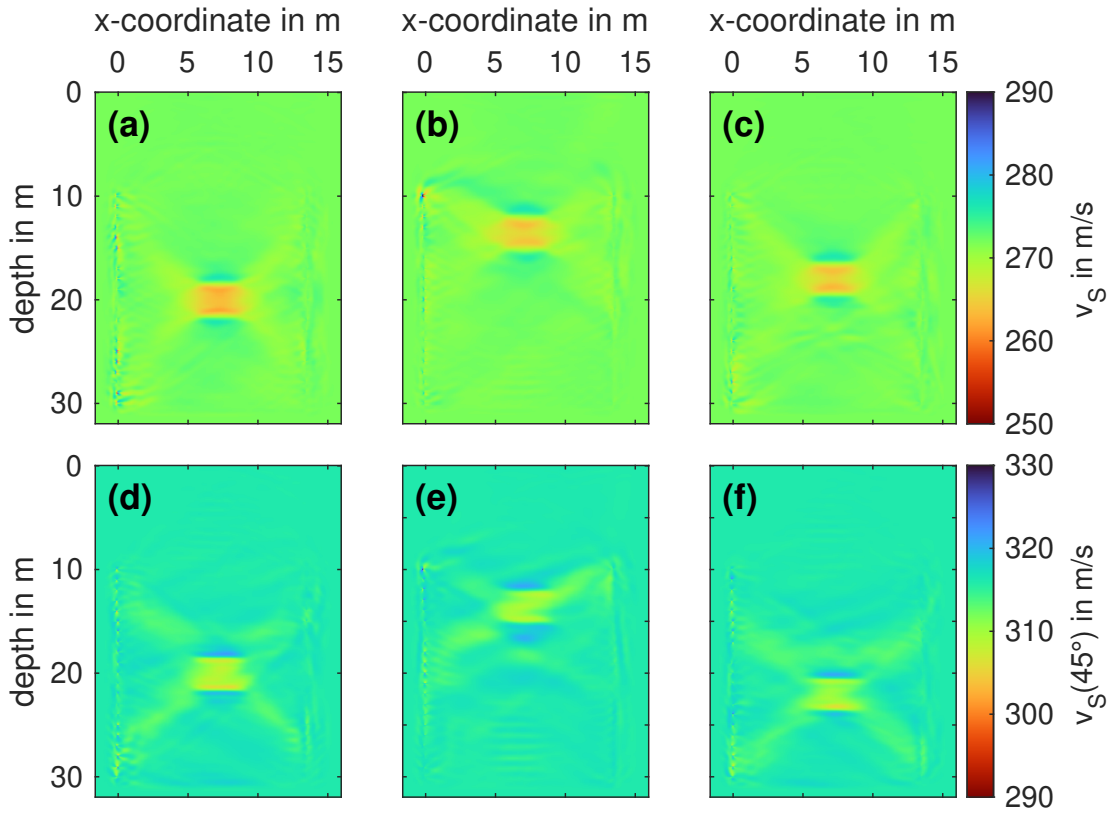

Figure 5.5: Inverted anisotropic SV-wave velocity models. The upper row shows the results for the vertical SV-wave velocity, the lower row those for the SV-wave velocity in a 45° direction. The models (a) and (d) depict the reconstruction of a square anomaly that get maximum illumination. The aperture test results in (b) and (e) reveal that the anomaly in the $v_{\mathrm{SV}}(45°)$ model can be reconstructed less well than the one in the v_{SV} model. Finally, the crosstalk test for the SV-wave velocities in (c) and (f) shows no significant influence of one parameter on the other.

Figure 5.5(a) and (d) show the results of the anisotropic inversion. Both the location and the extent of the anomalies can be recovered by the VTI inversion. However, the left and right edges of the v_{SV} anomaly are sharper than those of the $v_{SV}(45°)$ anomaly. While higher velocities are found right outside from where the anomaly edge at the right lower corner is located, lower velocities corresponding to the background velocity can be identified in the center of the actual edge. This effect has also been observed in a study by Hadden et al. (2019), though in the v_{SV} model instead. There, however, they use a parameterization in terms of the Thomsen parameter models ε and δ. Moreover, the true velocity values cannot be recovered completely for $v_{SV}(45°)$ with the closest value being 306 m/s, which still differs by about +2.5 m/s and thus less than 1% from the true value, whereas the minimum difference of the v_{SV} anomaly is only 1.00 m/s. While the velocity at the edges lies between the one of the anomaly and the background in case of the vertical SV-wave velocity, this transition is much less pronounced, i.e., the width of this zone is significantly smaller, in the reconstructed $v_{SV}(45°)$ model. Instead, there is a sharp velocity increase at the top and bottom edge of the anomaly location. Contrary to that, horizontal stripes can be identified further above and in particular below the anomaly in the $v_{SV}(45°)$ model, but not in the v_{SV} model where they seem to be smoothed. Furthermore, the width of those horizontal stripes decreases in the $v_{SV}(45°)$ model, whereas the higher velocity zones in the v_{SV} model extend towards the X-shaped artifacts that themselves extend towards the shallowest and deepest receiver (left-hand side) and source (right-hand side) locations. Again, the X-shaped artifacts have also been observed by Hadden et al. (2019), who also conducted VTI reconstruction tests with a rectangular anomaly in a crosswell setting. Overall, the $v_{SV}(45°)$ model exhibits more artifacts than the v_{SV} model. While in both models relatively extreme velocity values can be spotted at the receiver locations despite the tapers, the $v_{SV}(45°)$ model features, for instance, slightly increased velocities compared to the true background velocity between the deepest sources and receivers.

The inversion converges after 68 iterations, when the abort criterion of a relative misfit change smaller than 1% is met. The normalized L2 misfit as function of the iteration number is presented in Figure 5.3 (left) in red. A strong decrease down to about $7.9 \cdot 10^{-3}$ can be identified within the first twelve iterations. Then, the curve becomes flatter and reaches its minimum with $5.3 \cdot 10^{-4}$.

Contrary to what one would expect based on the quality of the reconstruction of the anomaly, the inverted waveforms fit the synthetic forward-modeled data perfectly by visual inspection (see Figure 5.6 (right)). A possible reason could be the slow convergence, such that the abort criterion of a relative misfit change less than 1% is fulfilled after a smaller number of iterations compared to the isotropic inversion. On top of that, geophysical inversion problems always exhibit a certain ambiguity such that several models can explain the data equally well.

Comparing the waveforms that are generated based on the true models with the final inversion results (see Figure 5.6 (right)), shows that the waveforms fit perfectly. Like in the isotropic aperture test, the initial models yield only differences in the shallowest traces.

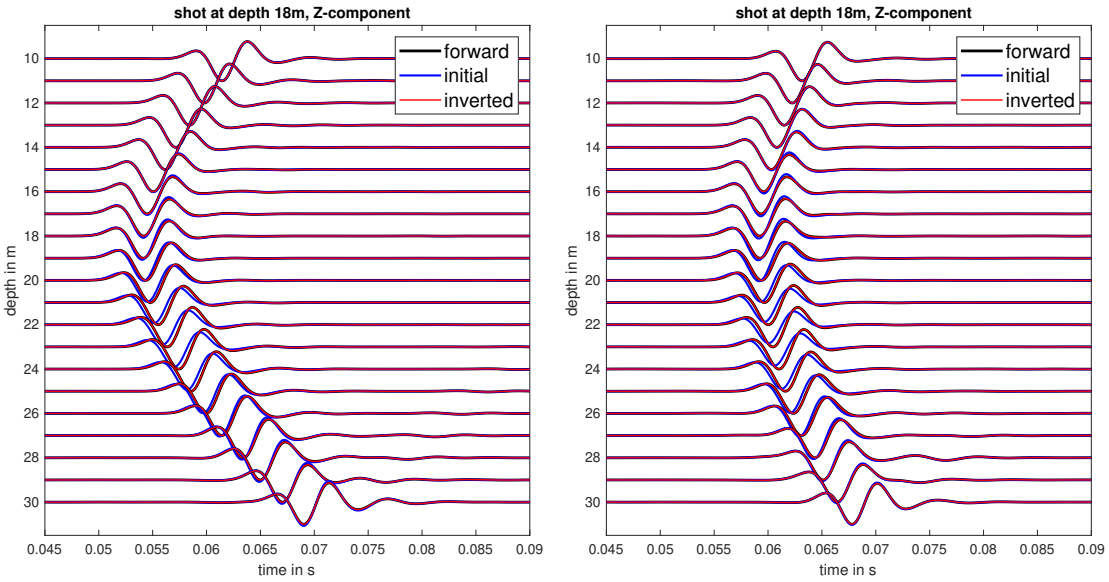

Figure 5.6: Seismograms based on true (black), starting (blue) and inverted (red) reconstruction test model. On the left-hand side the waveforms in the isotropic case are presented, on the right-hand side those of the VTI case.

5.1.3 Isotropic code and anisotropic models

In order to assess, whether an isotropic inversion is sufficient to reconstruct an anisotropic model assuming VTI symmetry, the anisotropic synthetic data is inverted using the isotropic code. As before, I only invert for the S-wave velocity model and apply circular source and receiver tapers.

Figure 5.7 (left) shows the inverted S-wave velocity model, which is clearly dominated by extreme values at the receiver (left-hand side) and the source (right-hand side) positions. Apart from that, the X-shaped artifacts with a slightly increased velocity compared to the background can be identified. The anomaly, however, can only be guessed to be in the center of the X-shaped artifact.

The inversion stops after only six iterations because the step length estimate fails. The reason why the inversion does not properly converge becomes apparent through a comparison of the waveforms in Figure 5.7 (right). While the onset times of the forward-modeled synthetic data and the waveforms based on the initial model almost match around the source depth, they differ by more than half a period at the shallowest and deepest receivers (see also chapter 4). This phenomenon is known as cycle skipping and prohibits a proper convergence of the inversion towards the global minimum.

5.1.4 VTI tomography model as background model

Instead of using a homogeneous background and starting model, the anisotropic tomography models are now used in this place. The same SV-wave velocity anomaly as above in the homogeneous VTI model is inserted at the same location. The models are shown in Figure 5.8. The inversion procedure of inverting for the SV-wave velocity models only while the P-wave velocity models and the density model are kept constant remains, just like the application of source and receiver tapers.

Figure 5.9 illustrates the inversion result. Neither the anomaly in the v_{SV} model nor the one in the $v_{\mathrm{SV}}(45°)$ model can be recovered. Instead, both SV-wave velocity

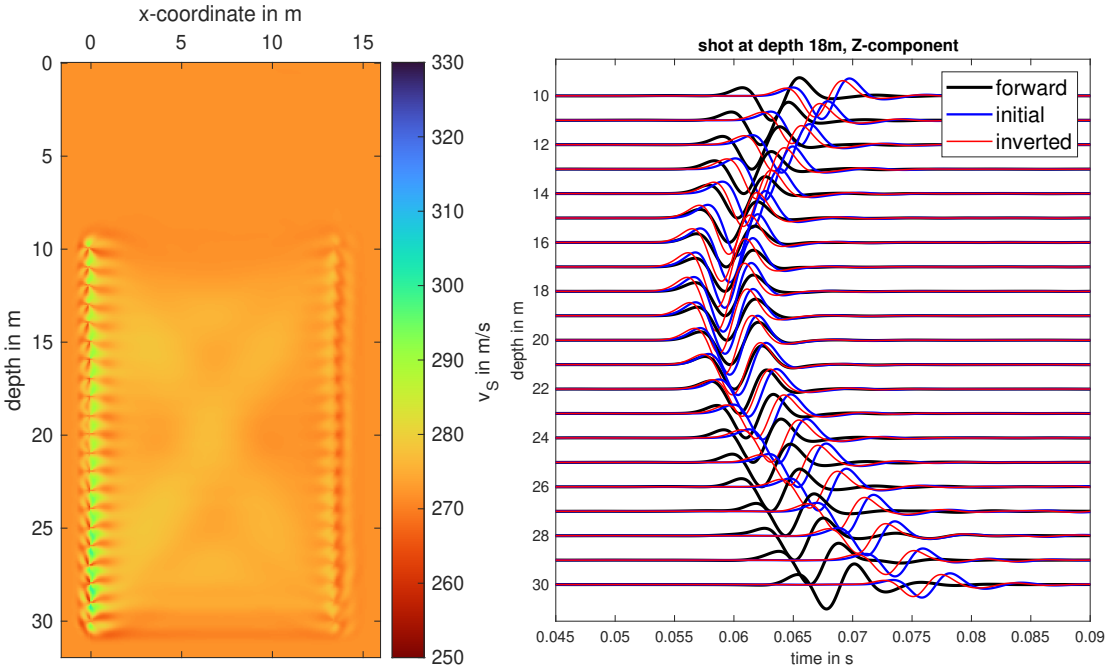

Figure 5.7: Isotropically inverted S-wave velocity model and waveforms from VTI data. Left: reconstructed S-wave velocity model, right: true, initial and inverted waveforms.

models show artificial structures towards the source and receiver locations such that the models become less smooth. Furthermore, comparably high velocities are recovered at the receiver positions and to a lesser extent at the source positions. The sole indicator that there might actually be another structure is the trench-like or triangular shape around the location of the anomaly which is better visible in the v_{SV} model than the $v_{SV}(45°)$ model. Along its right edge one might make out a low-velocity feature, where the lower right corner of the anomaly is located.

The inversion stops after 17 iterations because the step length estimation fails.

Similar to the isotropic inversion of the anisotropic data in subsection 5.1.3, cycle skipping can be identified at the traces in intermediate depth of 21 and 22 m. Moreover, the waveforms disagree quite significantly at later times of around 75 ms in the depth of the anomaly. At the trace at 10 m depth the inverted waveform even differs more from the true forward-modeled data than it does based on the initial tomography model. Contrary to that, the inversion improves the fit of the waveforms recorded at the three deepest receivers.

5.1.5 Comparison and conclusion

First of all, it has to be pointed out that the so-called "inverse crime" is committed by applying the same forward solver in the generation of the synthetic data based on the true models. However, this approach further restricts the inversion and allows to assess the performance of the VTI gradient parameterization compared to the isotropic one through the misfit evolution curves. In further studies, the issue of the inverse crime could be mitigated by adding artificial noise to the synthetic data that preferably has a similar spectrum as the field data. Even more appropriate would be to use another tool to generate synthetic data. Moreover, the coupling of P- and SV-waves is neglected because the anomaly is only introduced in the SV-wave velocity models. However, in order

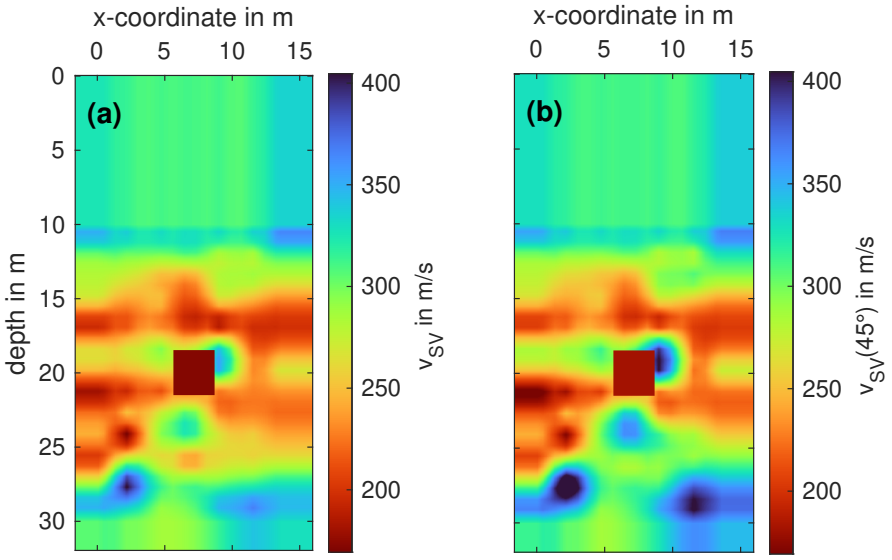

Figure 5.8: True VTI reconstruction test models with tomography model background. Figure (a) depicts the vertical SV-wave velocity model, (b) the one in a direction of 45°.

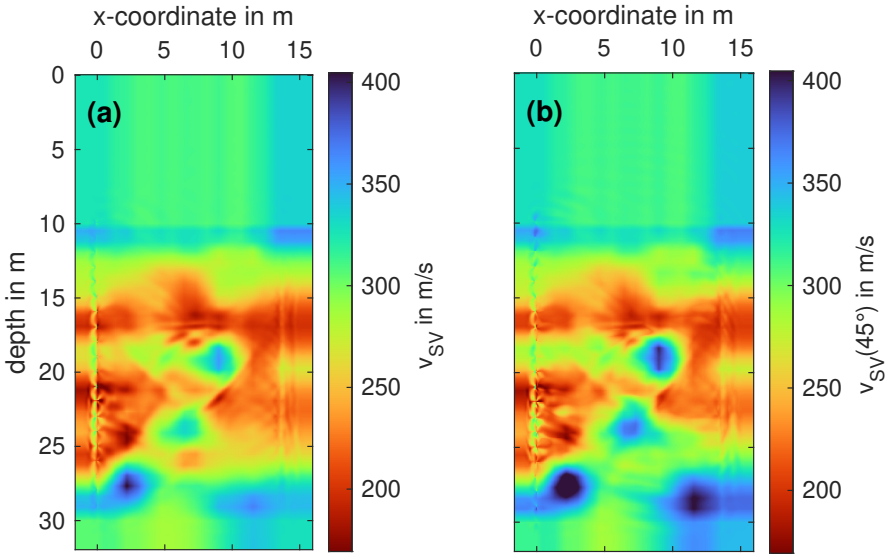

Figure 5.9: Inverted VTI reconstruction test models with tomography model background. Figure (a) depicts the vertical SV-wave velocity model, (b) the one in a direction of 45°. The anomaly can obviously not be reconstructed and artifacts at the source (right-hand side) and in particular the receiver locations (left-hand side) dominate the inverted model. Instead of reconstructing the anomaly, the background model is distorted by artifacts.

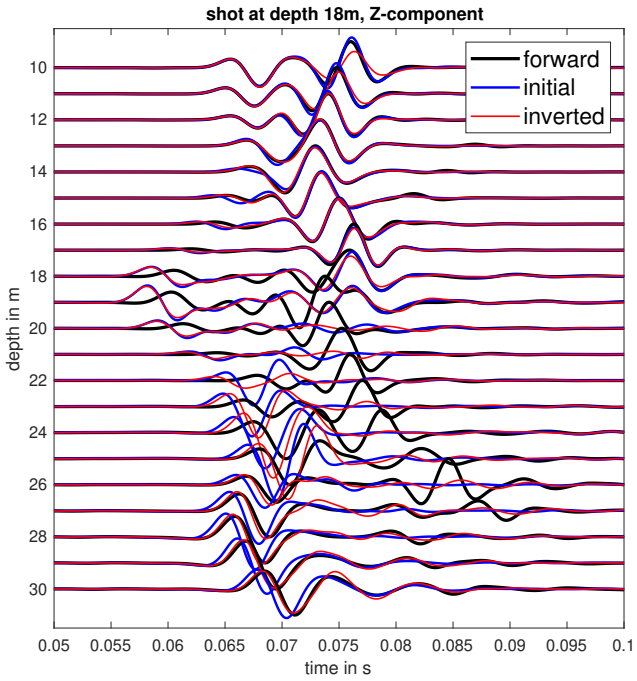

Figure 5.10: Seismograms based on true (black), starting (blue) and inverted (red) reconstruction test model with tomography model as background.

to simulate a situation as it was found in the traveltime tomography (see chapter 3), where almost no P-wave but strong S-wave anisotropy is observed, this approach is considered to be valid. The fact that the P-wave shows no anisotropy while the SV-wave does, follows from the high $v_{\mathrm{P}}/v_{\mathrm{SV}}$-ratio which controls the SV-wave anisotropy via the SV-wave anisotropy parameter $\nu = (v_{\mathrm{P0}}/v_{\mathrm{S0}})^2\ (\varepsilon - \delta)$ (von Ketelhodt et al., 2019)[6]. Possible crosstalk into the P-wave velocity and density models is avoided by keeping these models constant during the inversion.

Comparing the fully isotropic and the fully anisotropic inversion, the former yields a more satisfying result in the reconstruction of an S-wave low-velocity anomaly in intermediate source and receiver depths. This holds both for the shape of the anomaly and the velocity values. The two inversions, though, have in common that the vertical resolution is superior to the horizontal one, because the top and bottom edge are reconstructed better than the lateral edges. Furthermore, the velocities are recovered more accurately along horizontal stripes, especially at the upper and lower edge of the anomalies, both in the isotropic and the VTI case. Their lateral edges, though, are sharper in the isotropic case, while they are irregular in the anisotropic case. Hence, the vertical resolution of the isotropic inversion is superior to that of the VTI inversion. The horizontal resolution, however, is comparable. Finally, the anisotropic inversion produces more extreme values at the receiver locations than the isotropic inversion. In order to minimize the influence of those grid points, a stronger taper might be appropriate. Alternatively, the model updates could be restricted further because the true velocity values are known in these tests.

[6] In the publication the SV-wave anisotropy parameter is called σ instead of ν. However, σ is already used for the stress in this work.

The isotropic inversion with VTI data has shown that the isotropic theory is incapable to explain the data, because the difference in the non-vertical SV-wave velocity is too large to prevent cycle skipping. The latter yields convergence to a local instead of the global minimum of the misfit function. Consequently, an anisotropic inversion is required to reconstruct the true anisotropic model even in case of weak velocity anomalies.

The more complex setting with the anisotropic tomography models as background models does not allow to reconstruct the anomaly as well. Again, the inversion does not converge to the global minimum of the misfit function.

Thus, the last two reconstruction tests demonstrate the importance of a suitable starting model and proper assumptions about the subsurface to accurately model the data.

5.2 Aperture tests

The aperture here refers to the spatial extent to which a subsurface feature can be moved with respect to the acquisition geometry in a crosswell setting without loss of resolution in its reconstruction. It depends on the direction a wave approaches the velocity anomaly. Due to the directional dependency of the wave velocity in anisotropic media, an anisotropic inversion is expected to perform better than an isotropic one in case of an irregular illumination of an anomaly.

The effect of a changed aperture and the angular dependency of the S-wave velocity is studied, repeating the tests from above, but this time with the anomaly's upper edge in a depth of only 12.00 m. Hence, the anomaly is placed such that only two sources and receivers are located above it. This reduces the number of waves that propagate through it from above, but increases those that originate below the anomaly. Thus, the angle at which the waves from greater depth approach the lower right corner of the anomaly is reduced to about 23° minimum and the proportion of waves from shallower depths is increased to about 78° maximum with respect to the upper left corner. By this the resolution in the vertical direction should be further increased, while the horizontal resolution is expected to deteriorate in the isotropic case. For the VTI case, however, the horizontal resolution should be superior to the isotropic one, because the SV-wave velocity in a 45° direction is taken into account and thus contains additional information on the subsurface structure. Nevertheless, the advantageous directional dependency of the wave velocity in the VTI case might be reflected less than expected because this goes along with an additional parameter that has to be reconstructed. On top of that, I expect that the overall resolution is worse compared to the reconstruction tests because the anomaly is less well illuminated from above.

5.2.1 Isotropic code and isotropic models

Again, I start with the investigation of the fully isotropic case. The true isotropic S-wave velocity model is shown in Figure 5.1(b). As before in the reconstruction tests, circular tapers are applied at the source and receiver positions to prevent instabilities in the simulation.

Figure 5.5(b) shows the result of the inversion. The anomaly can be resolved well in terms of its location, extent and shape. Contrary to the expectation, the vertical

and horizontal resolution appear to be of the same quality as in the reconstruction test. The minimum difference to the true anomaly value is less than $-1\,\mathrm{m/s}$. Moreover, the recovered velocities are even closer to the true anomaly velocity compared to the reconstruction test. The features like horizontal stripes and X-shaped artifacts appear once again in the inverted model. The X-shaped artifacts, however, are complemented by additional branches such that they not only extend to the outer source and receiver locations, but also towards the free-surface at an angle similar to the ones towards the deepest source and receiver. Overall, on the one hand there are more artifacts in the inverted model if the anomaly is not located in the center of sources and receivers depths and the background model is disturbed towards velocities slightly too high. On the other hand, the recovered velocities at the grid points, where the anomaly is located, are closer to the true value. Regarding the resolution, it can be concluded that the changed aperture does not manifest itself in a reduced or increased resolution, but instead in the form of more artifacts.

The inversion requires 101 iterations to converge and stops because it reaches the pre-defined abort criterion of a relative misfit change of less than 1%. The normalized L2 misfit evolution as a function the iteration number is shown in Figure 5.3 (center) in black. Compared to the reconstruction test, the misfit decrease is smoother in the sense that it is not as steep in the beginning and does not have a significant kink. The final normalized misfit is $1.8{\cdot}10^{-4}$ and thus larger than the one obtained in the reconstruction test, which is not surprising after the discussion of the artifacts in the background model.

As in the reconstruction test, the inverted waveforms fit the forward-modeled synthetic data perfectly (see Figure 5.11 (left)). The waveforms based on the completely homogeneous starting only differ at the shallowest receivers as the anomaly is located at shallow depth. Again, a difference in the onset time between the true and initial model waveforms cannot be identified.

5.2.2 Anisotropic code and anisotropic models

Like in the reconstruction test, the low-velocity anomalies of the two SV-wave velocity models are placed at the same position with the top edge in 12 m depth (see Figure 5.4(b) and (e)). Just like in the other inversions, circular tapers are applied at the source and receiver positions.

The inversion results for the v_{SV} and the $v_{\mathrm{SV}}(45°)$ model are presented in Figure 5.5 (b) and (e), respectively. Compared to the reconstruction test, the anomalies are less well resolved with respect to their shape and velocity values in both SV-wave velocity models. The vertical velocity closest to the actual velocity is about 1% larger than the true value. Nevertheless, the anomaly in the v_{SV} model is recovered more satisfyingly regarding its shape as the upper and lower edges are more prominent in the sense that they extend over the actual horizontal width of the anomaly. The vertical edges, though, are less sharp than in the reconstruction test, i.e., the velocity reduction spreads further in lateral direction closer towards the left edge's center, while the higher background velocity penetrates the square shape from the right. In contrast to the vertical velocity model, the closest recovered value of the $v_{\mathrm{SV}}(45°)$ anomaly differs by about 5 m/s and thus less than 2% from the true value. Furthermore, the anomaly tends to extend towards the upper right and lower left of the source and receiver spreads from its corners, while it lacks some extent in the other diagonal direction. Thus, the X-shape effect is

less symmetric than before in the reconstruction test and also the isotropic case. It can be assumed that these effects arise from the directional dependency of the velocities in the VTI case. As the phase angle is larger for waves that originate in shallow depth in the source borehole, it seems reasonable that the effect of reduced velocities in that direction is apparent in the $v_{SV}(45°)$ model but not in the v_{SV} model for the given location of the anomaly. This effect might to a lesser extent also be identified along the other diagonal in the reconstruction test $v_{SV}(45°)$ model, because the anomaly cannot be placed exactly in the center due to the discretization. Additionally, the extreme velocity values are much lower in the aperture test, compared to the reconstruction test, at the shallowest receiver in the upper left compared to the other receiver positions.

The evolution of the misfit is shown in Figure 5.3 (center) in red. It decreases similarly to the isotropic inversion up to iteration 16. Then, the curve bends stronger than in the isotropic simulation and converges to the final normalized L2 misfit of $4.0 \cdot 10^{-3}$ at iteration 43 and as such remains above the order of 10^{-4}. The inversion terminates as the abort criterion of less than 1% of relative misfit change is reached.

A comparison of the waveforms is shown in Figure 5.11 (left). Again, no differences can be observed between the forward calculated waveforms based on the true model and the waveforms obtained in the inversion. Just like in the isotropic case, the anomaly only has an influence on the traces measured at shallow depth above 17 m.

5.2.3 Comparison and conclusion

A comparison of the fully isotropic and fully anisotropic inversions allows to draw the surprising conclusion that the isotropic scheme proves to yield better results in terms of both the vertical and the horizontal resolution as well as the recovery of the true velocity values. A reason for that might be that the anisotropic inversion requires an additional parameter reconstruction which implies a trade-off between the two SV-wave velocities. This will be investigated further in section 5.3. Besides, the reconstruction tests have already shown the inferior convergence behavior of the VTI gradient with the given crosswell geometry and parameter values in the sense that the misfit stagnates earlier. Consequently, the abort criterion regarding the relative misfit change is fulfilled after fewer iterations. A hypothesis to explain this observation is that the approximation that is used both in the $v_{SV}(45°)$ formula (see Equation 2.85) and the derivation of the VTI gradients (see subsection 2.3.3) prohibits a stronger convergence and a better reconstruction. The perfect waveform fit can be explained by the fact that the software reads in the $v_{SV}(45°)$ model which is calculated based on the approximated formula given by Equation 2.85. Although the isotropic aperture test yields more artifacts than the reconstruction test, it is still superior compared to the anisotropic inversion which also shows a decreased quality of the reconstruction of the anomaly in the aperture model.

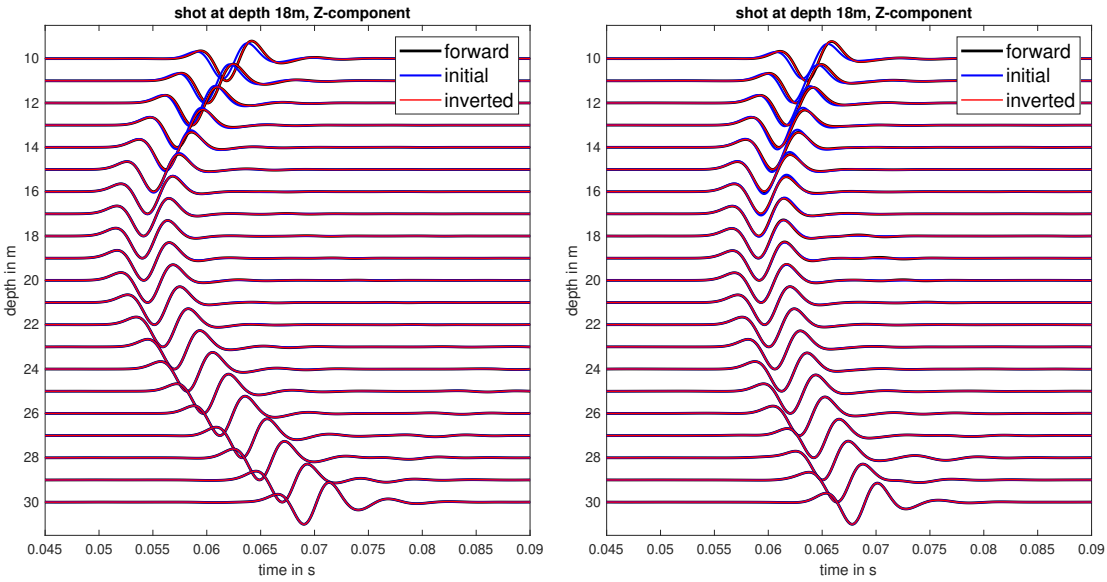

Figure 5.11: Seismograms based on true (black), starting (blue) and inverted (red) aperture model. On the left-hand side the waveforms in the isotropic case are presented. On the right-hand side the waveforms of the VTI case are depicted.

5.3 Crosstalk

For the crosstalk test between the VTI SV-wave parameters, the anomaly in the v_{SV} and $v_{\mathrm{SV}}(45°)$ model is placed at two different locations (see Figure 5.4(c) and (f)). The upper edge of the anomaly in the v_{SV} model is hereby located in 16.48 m depth and the one in the $v_{\mathrm{SV}}(45°)$ model in 20.48 m depth. Thus, the two anomalies have a distance of 1.00 m.[7] Once again, for each shot, circular tapers with the shape of a log-function are applied at source and receiver positions.

The inversion results in Figure 5.5(c) and (f) reveal that the parameterization yields surprisingly little crosstalk between the SV-wave parameters. The reconstruction of the anomaly in the v_{SV} model is comparable to the one in the reconstruction test in subsection 5.1.2 and shows even less extreme velocity values at the receiver positions. The recovered velocity value approaches the true value with a minimum difference of 2 m/s. The reconstruction of the anomaly in the $v_{\mathrm{SV}}(45°)$ model, however, looks more like the one in the aperture test. The recovered velocity that is closest to the true value differs from it by about 3 m/s. Furthermore, another zone of lower velocities compared to the true background model can be identified above the anomaly which probably has to be associated with the anomaly in the v_{SV} model, even though the artifacts differ in shape and velocity value. Hence, the inversion exposes minor crosstalk from the v_{SV} parameter into the $v_{\mathrm{SV}}(45°)$ parameter model. A behavior like this is expected as the formula to calculate the parameter $v_{\mathrm{SV}}(45°)$ in Equation 2.85 includes the vertical SV-wave velocity v_{SV}. Moreover, the P-wave parameters, i.e., the vertical and horizontal P-wave velocity are contained. These, however, are kept constant in the inversion, while the SV-wave parameters are updated. In the end, this entails that four of the elastic constants, namely c_{11}, c_{13}, c_{33} and c_{55}, contribute to the $v_{\mathrm{SV}}(45°)$ parameter and the

[7] Note that the exact location of the lower edge of the v_{SV} anomaly is actually at 19.44 m depth due to the discretization of the model with $\Delta h = 0.08$ m.

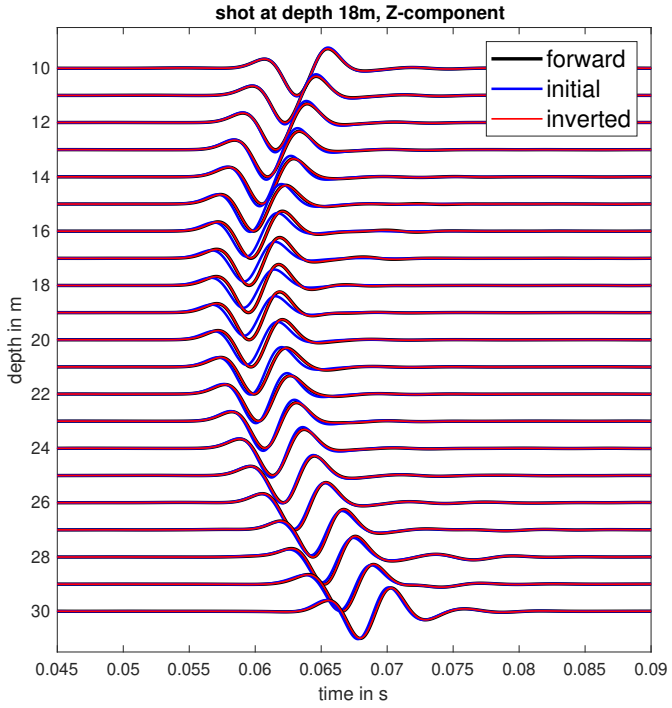

Figure 5.12: Seismograms based on true (black), starting (blue) and inverted (red) crosstalk test model. On the left-hand side the waveforms in the isotropic case are presented. On the right-hand side the waveforms of the VTI case are depicted.

gradient with respect to it. Contrary to that, v_{SV} and the gradient with respect to it only depends on c_{55}.

The inversion stops after 50 iterations at a normalized final misfit of $1.3 \cdot 10^{-3}$ because no proper step length can be found in the step length estimation that is used to determine the minimum of the misfit function. Initially, the misfit decays strongly until the curve bends at iteration eight and more so at about iteration 25.

A comparison of the waveforms in Figure 5.12 shows that the synthetics based on the true model can be exactly recovered from the starting model, which yields initial waveforms that differ from the true and inverted data over almost the entire depth range of receivers in their phase and amplitude. The onset times, tough, cannot be distinguished once again.

5.4 Conclusions from inversion tests and outlook

In conclusion, the inversion tests have shown that the isotropic inversion yields more satisfying results regarding the reconstruction and resolution of a low velocity anomaly even with a supposedly disadvantageous aperture. The conjecture that this is due to significant parameter crosstalk in the VTI case cannot be confirmed by the crosstalk test. Possible reasons for the reduced performance of the VTI inversion compared to the isotropic inversion might lie in the approximations of the $v_{\mathrm{SV}}(45°)$ parameter and the gradient calculation. Contrary to the initial expectation, the horizontal resolution in the VTI simulation cannot outperform the one of the isotropic inversion in case of a

reduced illumination. This, probably, also has to be attributed to the overall diminished quality of the reconstruction that does not allow for a profound comparison.

Apart from the emergence of instabilities with larger velocity anomalies, even weak velocity anomalies that are introduced into the anisotropic SV-wave tomography models lead to cycle skipping such that the tomography models without anomaly are no longer suitable as starting models. Similarly, an inadequate assumption about the isotropy of the subsurface cannot recover the true velocity model as an increase (or decrease) of the S-wave velocity might cause cycle skipping at those traces that are recorded, where the wavefront arrives neither from the vertical nor the horizontal direction. This demonstrates the importance of a suitable starting model and an appropriate assumption about the subsurface.

Further studies should treat the issue of the inverse crime by using a different tool to forward model the data. Besides, the coupling of P- and SV-wave anisotropy could be investigated. Apart from that, an additional data acquisition with reversed source and receiver boreholes might be helpful to obtain a better understanding of how much the geometry impacts the inversion in the VTI case with its directional dependence of phase velocities. In a field data study, however, this would increase the acquisition costs such that synthetic studies definitely have to be conducted in advance to assess the potential gain of information or the lack thereof. On top of that, field data would require a viscoelastic inversion because the Earth is not fully elastic but acts as low-pass filter damping the high frequencies in the wavefield with increasing travel distance. Concerning the inversion procedure, a more sophisticated approach, for instance, the joint inversion of P/SV- and SH-wave data, might be beneficial to better reconstruct anomalies in the VTI case. Hadden et al. (2019) show that, in their case, filtering the anisotropy parameters ε and δ with a Gaussian smoothing function improves the inversion results.

6. Conclusions

The present work analyzes the anisotropic wave propagation of SV-waves in a crosswell setting. The acquisition geometry offers a rare opportunity to obtain fine-scale information about the subsurface between the boreholes. On top of that, it is considered ideal to investigate the angular dependency of the wave velocity in anisotropic media.

My investigations are based on the findings of a traveltime tomography by von Ketelhodt et al. (2018, 2019). The field data was acquired at the southern border of the Elster sedimentary basin which became over-consolidated during the Elster-Saale glacial period. The horizontal layering and the experienced change of stress conditions are expected to yield VTI anisotropy. A joint inversion of SV- and SH-source data confirmed this as artifacts in the S-wave velocity model from a separate inversion could be reduced when applying a VTI assumption. The recovered anisotropy parameters are given in terms of the Thomsen parameters ε, δ and γ. These can be used to express the anisotropy in terms of the vertical P- and SV-wave velocities, the horizontal P-wave velocity $v_{\mathrm{P,hor}}$ and the SV-wave velocity in a 45° direction from the vertical $v_{\mathrm{SV}}(45°)$.

The forward simulations of the respective wavefields show that both anisotropy and viscoelasticity have a significant impact on the wavefield. Due to the increase or decrease of the SV-wave velocity with increasing phase angle up to 45°, cycle skipping can occur even in case of weak anisotropy if an isotropic subsurface is assumed in the forward calculations of the wavefield when it is actually anisotropic. Weak dispersion, that is introduced by the viscoelastic behavior of the subsurface, or a complex model, like the tomography model, further increase the probability for the emergence of cycle skipping such that even very weakly anisotropic models yield problems in case of unfitting assumptions about the subsurface properties. This demonstrates the importance of suitable starting models for FWI and how difficult it might be to find those in case of anisotropic, more realistic, i.e., viscoelastic, subsurface conditions.

While past studies on seismic anisotropy are often limited to a traveltime tomography or an acoustic anisotropic FWI, I derive the gradient for the VTI P/SV-case using a parameterization based on the velocities v_{P}, $v_{\mathrm{P,hor}}$, v_{SV} and $v_{\mathrm{SV}}(45°)$ as well as the density ρ, i.e., parameters in the same order of magnitude. The performance of the VTI FWI is investigated under the assumption of an elastic subsurface in a crosswell setting with velocity ratios based on the models which have been reconstructed through a traveltime tomography by von Ketelhodt et al. (2019). The inversion is further limited to the anisotropy of SV-waves as the P-wave velocities and the density model remain constant.

In order to study the VTI FWI's performance I run reconstruction tests of a low-velocity SV-wave anomaly in a homogeneous background model with both the isotropic

and the anisotropic *IFOS2D* code. Both the vertical and horizontal resolution are superior in the isotropic tests, even under disadvantageous illumination of the anomaly. The reasons for that remain so far unclear and require further investigations. A crosstalk test reveals surprisingly little crosstalk between the anisotropic SV-wave velocity parameters v_{SV} and $v_{SV}(45°)$.

Furthermore, it is confirmed that cycle skipping caused by an unfitting assumption about the subsurface properties actually prevents the inversion to converge to the global minimum of the misfit function such that the true model cannot be recovered from a simple homogeneous starting model without the anomaly. Similarly, a more complex background, as it is chosen with the anisotropic traveltime tomography model, does not allow a reconstruction of the anomaly as well, even under a VTI assumption.

All in all, the results suggest that a VTI inversion for SV-waves is appropriate if there are indications for the existence of a vertically transverse medium as the inversion might otherwise not converge to the global minimum. However, to obtain subsurface models of high resolution a more sophisticated inversion approach and a better handling of the, in parts, extreme velocity values at the source and receiver locations is probably required. Further studies, should also consider P-wave anisotropy along with the SV-wave anisotropy as those are not necessarily decoupled. This should also include crosstalk tests with all VTI P/SV-parameters. Finally, an application to field data would be necessary to assess the full potential of the VTI P/SV-case FWI.

Bibliography

Bai, T. and Tsvankin, I. (2016). Time-domain finite-difference modeling for attenuative anisotropic media. *Geophysics*, 81(2):C69–C77.

Bai, T., Tsvankin, I., and Wu, X. (2017). Waveform inversion for attenuation estimation in anisotropic media. *Geophysics*, 82(4):WA83–WA93.

Barnes, C., Charara, M., and Tsuchiya, T. (2008). Feasibility study for an anisotropic full waveform inversion of cross-well seismic data. *Geophysical Prospecting*, 56(6 SPEC. ISS.):897–906.

Bauer, K., Haberland, C., Pratt, R., Ryberg, T., Weber, M., and Mallik Working Group (2003). Crosswell seismic studies in gas hydrate-bearing sediments: P wave velocity and attenuation tomography. In *EGS - AGU - EUG Joint Assembly*, EGS - AGU - EUG Joint Assembly, page 12377.

Bécache, E., Fauqueux, S., and Joly, P. (2003). Stability of perfectly matched layers, group velocities and anisotropic waves. *Journal of Computational Physics*, 188(2):399–433.

Berryman, J. G. (1979). Long-wave elastic anisotropy in transversely isotropic media. *Geophysics*, 44(5):896–917.

Blanch, J. O., Robertsson, J. O., and Symes, W. W. (1995). Modeling of a constant Q: methodology and algorithm for an efficient and optimally inexpensive viscoelastic technique. *Geophysics*, 60(1):176–184.

Bohlen, T. (1998). *Viskoelastische FD-Modellierung seismischer Wellen zur Interpretation gemessener Seismogramme*. PhD thesis, Christian-Albrecht University Kiel.

Bohlen, T. (2002). Parallel 3-D viscoelastic finite difference seismic modelling. *Computers and Geosciences*, 28(8):887–899.

Brossier, R. (2009). Imagerie sismique à deux dimensions des milieux visco-élastiques par inversion des formes d'ondes : développements méthodologiques et applications. Technical report.

Bunks, C., Saleck, F. M., Zaleski, S., and Chavent, G. (1995). Multiscale seismic waveform inversion. *Geophysics*, 60(5):1457–1473.

Carcione, J. M., Kosloff, D., and Kosloff, R. (1988). Wave propagation simulation in a linear viscoacoustic medium. *Geophysical Journal*, 93(2):393–401.

Charara, M. and Barnes, C. (2016). Multi-parameter viscoelastic full waveform inversion of cross-well Seismic data. In *78th EAGE Conference and Exhibition 2016: Efficient Use of Technology - Unlocking Potential*, volume 2016, pages 1–5. European Association of Geoscientists and Engineers, EAGE.

Clayton, C. R. I. (2011). Stiffness at small strain: research and practice. *Géotechnique*, 61(1):5–37.

Courant, R., Friedrichs, K., and Lewy, H. (1928). Über die partiellen Differenzengleichungen der mathematischen Physik. *Mathematische Annalen*, 100(1):32–74.

Courant, R., Friedrichs, K., and Lewy, H. (1967). On the Partial Difference Equations of Mathematical Physics. *IBM Journal of Research and Development*, 11(2):215–234.

Crampin, S. (1984). An introduction to wave propagation in anisotropic media. *Geophysical Journal of the Royal Astronomical Society*, 76(1):17–28.

Dietze, M. (2007). Evaluierung von Feldmethoden zur Quantifizierung von Schadstoffminderungen im Fahnenbereich am Beispiel eines BTEX-Schadens. Technical report, Institut für Geowissenschaften der Universität Tübingen, Tübingen, Germany.

Fang, X., Fehler, M. C., and Cheng, A. (2013). Simulation of the effect of stress-induced anisotropy on borehole compressional wave propagation. *Geophysics*, 79(4):D205–D216.

Fletcher, R. (1964). Function minimization by conjugate gradients. *The Computer Journal*, 7(2):149–154.

Forbriger, T., Groos, L., and Schäfer, M. (2014). Line-source simulation for shallow-seismic data. Part 1: Theoretical background. *Geophysical Journal International*, 198(3):1387–1404.

Gallardo, L. A. and Meju, M. A. (2003). Characterization of heterogeneous near-surface materials by joint 2D inversion of dc resistivity and seismic data. *Geophysical Research Letters*, 30(13):1658.

Gallardo, L. A. and Meju, M. A. (2004). Joint two-dimensional DC resistivity and seismic travel time inversion with cross-gradients constraints. *Journal of Geophysical Research*, 109(B3):B03311.

Gardner, G. H., Gardner, L. W., and Gregory, A. R. (1974). Formation Velocity and Density - the Diagnostic Basics for Stratigraphic Traps. *Geophysics*, 39(6):770–780.

Gaucher, E., Azzola, J., Schulz, I., Meinecke, M., Dirner, S., Steiner, U., and Thiemann, K. (2020). Active cross-well survey at geothermal site Schäftlarnstraße.

Geotomographie GmbH (2021). Seismic borehole and surface equipment » Geotomographie GmbH.

Gholami, Y., Brossier, R., Operto, S., Prieux, V., Ribodetti, A., and Virieux, J. (2013). Which parameterization is suitable for acoustic vertical transverse isotropic full waveform inversion? Part 2: Synthetic and real data case studies from Valhall. *Geophysics*, 78:R81–R105.

Giroux, B. and Gloaguen, E. (2012). Geostatistical traveltime tomography in elliptically anisotropic media. *Geophysical Prospecting*, 60(6):1133–1149.

Gupta, I. N. (1973). Premonitory variations in S-wave velocity anisotropy before earthquakes in Nevada. *Science*, 182(4117):1129–1132.

Hadden, S., Pratt, R. G., and Smithyman, B. (2019). Anisotropic full-waveform inversion of crosshole seismic data: A vertical symmetry axis field data application. *Geophysics*, 84(1):B15–B32.

Hadden, S. M. and Pratt, R. G. (2017). Full waveform inversion of crosshole data in tilted transversely isotropic media. In *79th EAGE Conference and Exhibition 2017*. European Association of Geoscientists and Engineers, EAGE.

Helbig, K. (1979). On: "The reflection, refraction, and diffraction of waves in media with an elliptical velocity dependence", by Franklyn K. Levin (Geophysics , April 1978, p. 528–537.). *Geophysics*, 44(5):987–990.

Helbig, K. (1981). Systematic classification of layer-induced transverse isotropy. *Geophysical Prospecting*, 29(4):550–577.

Helbig, K. and Thomsen, L. (2005). 75-plus years of anisotropy in exploration and reservoir seismics: A historical review of concepts and methods. *Geophysics*, 70(6):9ND–23ND.

Ikelle, L. T. and Amundsen, L. (2005). *Introduction to Petroleum Seismology*. Society of Exploration Geophysicists.

Jaeger, J., Cook, N., and Zimmerman, R. (2007). *Fundamentals of Rock Mechanics*. Wiley.

Kamath, N. and Tsvankin, I. (2014). Elastic full-waveform inversion of transmission data in 2D VTI media. In *Society of Exploration Geophysicists International Exposition and 84th Annual Meeting SEG 2014*, pages 1157–1161. Society of Exploration Geophysicists.

Köhn, D., De Nil, D., Kurzmann, A., Przebindowska, A., and Bohlen, T. (2012). On the influence of model parametrization in elastic full waveform tomography. *Geophysical Journal International*, 191(1):325–345.

Komatitsch, D. and Martin, R. (2007). An unsplit convolutional perfectly matched layer improved at grazing incidence for the seismic wave equation. *Geophysics*, 72(5):SM155–SM167.

Krampe, V. (2018). *2D elastic full-waveform inversion of Love waves in vertically transversely isotropic media / Valérie Krampe - Karlsruher Institut für Technologie*. mastersthesis, Karlsruher Institut für Technologie (KIT).

Kühn, F. (2018). Ultrasound medical imaging using 2d viscoacoustic full-waveform inversion - Medizinische Bildgebung mit Ultraschall unter Nutzung der 2d viskoakustischen Wellenfeldinversion. Master's thesis, Karlsruher Institut für Technologie (KIT).

Levander, A. R. (1988). Fourth-order finite-difference P-SV seismograms. *Geophysics*, 53(11):1425–1436.

Liu, H.-P., Anderson, D. L., and Kanamori, H. (1976). Velocity dispersion due to anelasticity; implications for seismology and mantle composition. *Geophysical Journal International*, 47(1):41–58.

Liu, Q. and Tromp, J. (2006). Finite-frequency kernels based on adjoint methods. *Bulletin of the Seismological Society of America*, 96(6):2383–2397.

Liu, Y., Teng, J., Xu, T., Badal, J., Liu, Q., and Zhou, B. (2017). Effects of Conjugate Gradient Methods and Step-Length Formulas on the Multiscale Full Waveform Inversion in Time Domain: Numerical Experiments. *Pure and Applied Geophysics*, 174.

Mari, J.-L. and Vergniault, C. (2020). *Well seismic surveying and acoustic logging*. EDP Sciences.

McMechan, G. A. (1983). Seismic tomography in boreholes. *Geophysical Journal of the Royal Astronomical Society*, 74(2):601–612.

Moczo, P., Kristek, J., and Halada, L. (2004). *The finite-difference method for seismologists. An introduction.* Comenius University, Bratislava.

Nishizawa, O. (1982). Seismic velocity anisotropy in a medium containing oriented cracks-transversely isotropic case. *Journal of Physics of the Earth*, 30(4):331–347.

Nocedal, J. and Wright, S. (1999). Numerical Optimization. page 636.

Paige, C. C. and Saunders, M. A. (1982). LSQR: An Algorithm for Sparse Linear Equations and Sparse Least Squares. *ACM Transactions on Mathematical Software (TOMS)*, 8(1):43–71.

Pei, Z., Fu, L. Y., Sun, W., Jiang, T., and Zhou, B. (2012). Anisotropic finite-difference algorithm for modeling elastic wave propagation in fractured coalbeds. *Geophysics*, 77(1):C13–C26.

Plessix, R.-E. (2006). A review of the adjoint-state method for computing the gradient of a functional with geophysical applications. *Geophysical Journal International*, 167(2):495–503.

Plessix, R. E. and Mulder, W. A. (2004). Frequency-domain finite-difference amplitude-preserving migration. *Geophysical Journal International*, 157(3):975–987.

Polak, E. and Ribiere, G. (1969). Note sur la convergence de méthodes de directions conjuguées. *ESAIM: Mathematical Modelling and Numerical Analysis - Modélisation Mathématique et Analyse Numérique*, 3(R1):35–43.

Pratt, R. G., Plessix, R. E., and Mulder, W. A. (2005). *Seismic waveform tomography: Crosshole results from the Nimr field in Oman*, pages 714–717.

Rao, Y. and Wang, Y. (2005). Crosshole seismic tomography: working solutions to issues in real data travel time inversion. *Journal of Geophysics and Engineering*, 2(2):139–146.

Robertsson, J. O., Blanch, J. O., and Symes, W. W. (1994). Viscoelastic finite-difference modeling. *Geophysics*, 59(9):1444–1456.

Singh, S., Tsvankin, I., and Zabihi Naeini, E. (2020). Full-waveform inversion with borehole constraints for elastic VTI media. *Geophysics*, 85(6):R553–R563.

Sourbier, F., Operto, S., Virieux, J., Amestoy, P., and L'Excellent, J. Y. (2009a). FWT2D: A massively parallel program for frequency-domain full-waveform tomography of wide-aperture seismic data-Part 1. Algorithm. *Computers and Geosciences*, 35(3):487–495.

Sourbier, F., Operto, S., Virieux, J., Amestoy, P., and L'Excellent, J. Y. (2009b). FWT2D: A massively parallel program for frequency-domain full-waveform tomography of wide-aperture seismic data-Part 2. Numerical examples and scalability analysis. *Computers and Geosciences*, 35(3):496–514.

Tarantola, A. (1984). Inversion of Seismic Reflection Data in the Acoustic Approximation. *Geophysics*, 49(8):1259–1266.

Thomsen, L. (1986). Weak elastic anisotropy. *Geophysics*, 51(10):1954–1966.

Tonn, R. (1989). Comparison of seven methods for the computation of Q. *Physics of the Earth and Planetary Interiors*, 55(3-4):259–268.

Tromp, J. (2020). Seismic wavefield imaging of Earth's interior across scales. *Nature Reviews Earth & Environment*, 1(1):40–53.

Tsvankin, I. (2001). *Seismic Signatures and Analysis of Reflection Data in Anisotropic Media, Volume 29 - 1st Edition*. Elsevier B.V.

Virieux, J. (1984). SH- wave propagation in heterogeneous media: velocity- stress finite-difference method. *Geophysics*, 49(11):1933–1942.

Virieux, J. (1986). P- SV wave propagation in heterogeneous media: velocity- stress finite-difference method. *Geophysics*, 51(4):889–901.

Virieux, J. and Operto, S. (2009). An overview of full-waveform inversion in exploration geophysics. *Geophysics*, 74(6):WCC1–WCC26.

Voigt, W. (1910). *Lehrbuch der Kristallphysik (mit Ausschluss der Kristalloptik)*. Leipzig, Berlin, B.G. Teubner.

von Ketelhodt, J. K., Fechner, T., Manzi, M. S., and Durrheim, R. J. (2018). Joint inversion of cross-borehole P-waves, horizontally and vertically polarized S-waves: Tomographic data for hydro-geophysical site characterization. *Near Surface Geophysics*, 16(5):529–542.

von Ketelhodt, J. K., Manzi, M. S., Durrheim, R. J., and Fechner, T. (2019). Seismic vertical transversely isotropic parameter inversion from P- and S-wave cross-borehole measurements in an aquifer environment. *Geophysics*, 84(3):D101–D116.

Warner, M., Ratcliffe, A., Nangoo, T., Morgan, J., Umpleby, A., Shah, N., Vinje, V., Štekl, I., Guasch, L., Win, C., Conroy, G., and Bertrand, A. (2013). Anisotropic 3D full-waveform inversion. *Geophysics*, 78(2):R59–R80.

Wu, C. and Harris, J. M. (2003). Borehole seismic modeling with inclusion of tube waves and other tube-wave-related arrivals. *SEG Technical Program Expanded Abstracts*, 22(1):2239–2242.

Zhang, F., Juhlin, C., Cosma, C., Tryggvason, A., and Pratt, R. (2012). Cross-well seismic waveform tomography for monitoring CO2 injection: A case study from the Ketzin Site, Germany. *Geophysical Journal International*, pages 629–646.

Zhou, B., Greenhalgh, S., and Green, A. (2008). Nonlinear traveltime inversion scheme for crosshole seismic tomography in tilted transversely isotropic media. *Geophysics*, 73(4):D17–D33.

Zhu, Y. and Tsvankin, I. (2006). Plane-wave propagation in attenuative transversely isotropic media. *Geophysics*, 71(2):T17–T30.